Forschungszentrum Karlsruhe
in der Helmholtz-Gemeinschaft

Wissenschaftliche Berichte

FZKA 7504

Modelling of Boundary Plasma in TOKES

Y. Igitkhanov, S. Pestchanyi, I. Landman

Institut für Hochleistungsimpuls- und Mikrowellentechnik
Programm FUSION
Association EURATOM/Forschungszentrum Karlsruhe

Dezember 2009

Forschungszentrum Karlsruhe
in der Helmholtz-Gemeinschaft
Wissenschaftliche Berichte

FZKA 7504

Modelling of Boundary Plasma in TOKES

Yu. Igitkhanov
S. Pestchanyi
I. Landman

Institut für Hochleistungsimpuls- und Mikrowellentechnik
Programm Fusion
Association EURATOM-FZK

Forschungszentrum Karlsruhe GmbH, Karlsruhe

2009

Forschungszentrum Karlsruhe GmbH
Postfach 3640, 76021 Karlsruhe

Mitglied der Hermann von Helmholtz-Gemeinschaft
Deutscher Forschungszentren (HGF)

ISSN 0947-8620

urn:nbn:de:0005-075042

Abstract

The main purpose of this report is the development of analytical and numerical transport models of tokamak plasmas, suitable for implementation into the integrated transport code TOKES [1-4]. Therefore this work is presented as an executive guideline for numerical implementation. The tokamak edge plasma in reactor configurations is expected to be rather thin outmost area with strong radial plasma gradients inside the separatrix and the area outside the separatrix, a scrape-off layer (SOL), with open magnetic field surfaces, terminated at the divertor plates. The region beyond the separatrix plays an important role because it serves as a shield, protecting the wall from the hot plasma and bulk plasma from the penetration of impurities and because it is mostly affected by transients. The transport model, proposed here, provides plasma density, temperature and velocity distribution along and across the magnetic field lines in bulk and the edge plasma region. It describes the dependence of temperature and density at the separatrix on the plasma conditions at the plate and the efficiency of the divertor operation in detached or attached conditions, depending on power and particle sources. The calculation gives eventually the power and particle loads on the divertor plates and side walls.

During numerical implementation some simple models, allowing an analytical solution, were developed and used for comparison and checking. Some parts of the transport models were also benchmarked with experimental data from various tokamaks.

In the frame of this work the following tasks have been completed:

- The transport model with neoclassical and anomalous coefficients for bulk plasma and 2D transport model for the SOL have been prepared and implemented into the TOKES code. The coefficients are suitable for description of stationary plasma processes in the bulk and edge tokamak plasmas.
- The model of pedestal formation at the plasma edge in H-mode operation was implemented in TOKES. The model based on power scaling for L to H transition and includes the mitigation of turbulence at the edge once the flowing power exceeds the H-mode onset threshold.
- The model of the Edge Localized Mode oscillation based on ballooning mode instability is implemented into code.
- The boundary conditions for fluid equations at the divertor plates and at the main chamber wall are formulated and implemented into the integrated code.
- Analyses of available experiments and benchmarking with simple analytical solutions in respect to SOL transport phenomena have been provided. Application for ITER is described.

Modellierung des Randplasmabereichs in TOKES

Zusammenfassung

Der Hauptzweck dieses Berichts ist die Entwicklung von analytischen und numerischen Transportmodellen für Tokamak Plasmen, passend zur Implementierung in den integrierten Transportcode TOKES [1-4]. Deshalb wird diese Arbeit als eine Exekutivrichtlinie für die numerische Implementierung präsentiert. Wie man erwartet, ist das Tokamak Randschichtplasma in Reaktorkonfigurationen ein ziemlich dünnes, äußeres Gebiet mit starken radialen Plasmagradienten innerhalb der Separatrix und des Gebietes außerhalb der Separatrix (sogenannte „scrape-off layer“ Schicht, SOL) mit offenen Magnetfeldoberflächen, begrenzt durch die Divertorplatten. Der Plasmabereich außerhalb des Separatrix spielt eine wichtige Rolle, weil er größtenteils von ELM-Instabilitäten und Plasmazusammenbruch-Ereignissen betroffen wird und weil er als ein Schutzschild dient, der die Wand vor dem heißen Plasma und das Zentralplasmagebiet vor Verunreinigungen schützt. Das hier vorgeschlagene Transportmodell stellt Plasmadichte, Temperatur- und Geschwindigkeitsprofile entlang und quer zu den Magnetfeld-Linien im Zentral- und im Randplasma zur Verfügung. Es beschreibt die Abhängigkeit der Temperatur und Dichte an der Separatrix von den Plasmabedingungen an den Divertorplatten und der Leistungsfähigkeit des Divertors in den „detached“ oder „attached“ Regimen, abhängig von der Leistung und den Teilchen-Quellen. Die Berechnung ergibt schließlich die Leistungs- und Teilchenbelastung auf den Divertorplatten und auf der Wand. Zur numerischen Implementierung im Code wurden einige einfache Modelle, die analytische Lösungen erlauben, entwickelt und zum Vergleich und für die Überprüfung verwendet. Einige Teile der Transportmodelle wurden auch mit experimentellen Daten von verschiedenen Tokamaks validiert.

Im Rahmen dieser Arbeit wurden die folgenden Aufgaben fertiggestellt:

- Das Transportmodell mit neoklassischen und anomalen Transportkoeffizienten für das Zentralplasma und das 2D Plasmatransportmodell für die SOL sind entwickelt und in den TOKES-Code eingebaut worden. Die Koeffizienten sind zur Beschreibung stationärer Tokamak-Plasmaprozesse im Zentrum und am Rand geeignet.
- Das Modell der Podest-Bildung am Plasmarand in der H-Mode wurde in TOKES implementiert. Das Modell basiert auf der Leistungsskalierung für den L-H-Mode-Übergang und schließt die Abschwächung der Turbulenz am Rand ein, die stattfindet, sobald der Leistungsfluss die H-Moden-Schwelle überschritten hat.
- Das Modell der Edge Localized Mode Schwingung basiert auf der Ballooning-Instabilität und wurde in den Code eingebaut.
- Die Randbedingungen für Transportgleichungen an den Divertorplatten und an der Gefäßwand wurden formuliert und in den integrierten Code implementiert.
- Analysen von existierenden experimentellen Ergebnissen und die Vergleiche mit analytischen Lösungen hinsichtlich der SOL-Transportergebnisse, werden zur Verfügung gestellt. Die Anwendungen für ITER sind beschrieben.

Table of content

I. Introduction

Analysis of the performance of a tokamak has traditionally focused separately on three distinct areas of the plasma; the regions with closed magnetic flux surfaces, referred to as the core or bulk plasma and the pedestal area, bordering with separatrix. The region outside the last closed flux surface is referred as the scrape-off layer (SOL). The core region has historically received more attention since the performance of the tokamak plasma is measured by the maximum densities and temperatures which can be achieved in that region. Analysis of the core performance takes many forms.

The simplest analysis is determination of empirical scaling laws for the energy confinement time. These laws permit identification of the key operational parameters, and allow meaningful comparison of the performance of a variety of devices. This analysis approach has been used as a design tool for large generations of tokamaks, and is currently being used as guidance for the design of ITER [5].

A second analysis scheme is transport analysis where detailed measurements of the radial profile of density and temperature are combined with determination of the heating and particle source profiles to determine the perpendicular transport diffusivities for particles and thermal energy. This analysis permits determination of the radial profile of the transport diffusivities, and hence is viewed as the first step in reaching understanding of the physics of the transport processes. The plasma parameters are typically assumed to be constant along magnetic flux surfaces, permitting 1-D analysis. Typically, these codes used the poloidal flux surfaces to define the "radial" coordinate. Since these surfaces do not have to be simple circles, but can be shaped, the resulting geometry is referred to as 1.5-D. Uncertainty in the details of the source profiles, and questions about the applicability of the 1.5-D assumption limits this analysis to regions well inside the last closed flux surface.

The radial transport pattern in bulk plasma consists of subdominant neoclassical transport, which is in our case is simulated not by the conventional routine NCLASS [6], but in the form of analytical formulas [7-9]. This allows one readily introduce in future the corrections in transport coefficients due to strong plasma gradients in pedestal region, where the applicability of standard neoclassical expressions fails [10].

A significant progress has been made in determination of the anomalous transport diffusivities from fundamental physics models, which allow one predictive calculations of the core and pedestal region. Due to the intrinsic complexity of plasma turbulence the transport formulas derived from parameterizations of basic non-linear computer simulations contain

modelling assumptions. These formulas were validated against the transport coefficients, determined experimentally from existing tokamaks. Two transport models are recognized as a dominant transport models in bulk plasmas. It is the gyro-Bohm transport models based on ion temperature gradient (ITG) transport in ions [8,9] and in electrons the phenomenological model, based on electron temperature gradient [11,12]**.**

Analyse of the transport mechanisms at the pedestal region show the large contribution of magneto electrostatic turbulence. The H-mode is believed to be obtained by shear stabilization of turbulence in the pedestal region of a tokamak [13, 14]. For the modeling of pedestal formation we have chosen an approach, where transport mitigation down to neoclassical level occurs, when power flux across the pedestal region exceeds the L to H transition power threshold.

Analysis of the plasma behavior on the open magnetic field lines in the SOL region shows that plasma is toroidally symmetric, but is 2-D in character. Typically, the models use the Braginskii fluid model [15] for plasma transport, with the perpendicular transport, treated as anomalous. Similarly, impurity radiation plays a key role in power dissipation in the SOL, hence the 2-D models have developed techniques of simulating multi-species plasmas, including both intrinsic impurities (typically carbon) and impurity species introduced to enhance radiation. The presence of numerous multiply charged ions in the edge (scrape-off layer) of diverted tokamak plasma makes it difficult and time-consuming to accurately model the transpoprt processes in this region. A new model was developed, where the separate charge states of a given isotope can be accurately replaced by a set of appropriately averaged density, temperature, mass and heat flow equations representing a fictitious single reduced charge state [16,17]. These models are generally applied to divertor tokamaks, where the last closed flux surface corresponds to the magnetic separatrix. But these models must be also recognized in pedestal regions, where the 2-D nature of the plasma extends into the closed flux surfaces. This is particularly important for calculation of poloidal asymmetry of radiation during the mitigation of the disruption by massive gas injection. It has become increasingly apparent that the two regions of the plasma, the core and SOL, are not truly independent.

The development of the plasma transport in TOKES comprise of three models. First is the subdominant neoclassical transport for electrons and ions for tokamak plasma, based on Hinton and Heseltine model [7]. The turbulent transport, dominant in the bulk H-mode plasma is simulated by ITG and ETG type turbulent models. The SOL and divertor region is dominated by Bohm type transport arose and classical fluid transport along the magnetic field lines.

The boundary plasma region in tokamak device is conventionally defined as an external plasma volume, which consist of a pedestal region inside the separatrix and the region beyond the last closed flux surface (LCFS), where plasma is not magnetically confined and contacting with the in-vessel structures. The regions beyond the separatrix comprise the scrape-off layer (SOL) and the divertor plasma region. The advantage of the TOKES code is the inherent capability to simulate simultaneously bulk and edge plasma in spite of difference in geometry and time scales [2-4].

The application of TOKES to ITER is currently expected in several issues. Simulation of impurity transport in ELMy SOL due to enhancement of sputtering during small (mitigated) ELMs will define the lifetime of divertor plates, radiation power load on Be wall and ultimate balk plasma contamination level. This also includes effect of core plasma screening due to entrainment of impurities by ELMs and determination of the tolerable ELM size and frequency. Another task which can be tackled is related to simulation of massive gas injection for ITER.

The physics issues considered below are presented in such extend, which are required for the purpose of modeling. For additional information the references are applied. All quantities below in "practical" formulas are in MKS units except temperatures expressed in eV and ion mass (m_i) expressed in units of proton mass, $\mu = m\ / m_p$; B in Tesla, Z is the charge state; Boltzmann's constant $k_b = 6.25 \cdot 10^{24} eV/(s \cdot MW)$.

II. Neoclassical Transport Model for bulk and pedestal region in TOKES

The neoclassical transport coefficients for large aspect-ratio tokamaks in several regimes of collisionality were used in the form, suitable for numerical implementation. To be most useful, the results were used in the form of continuous function of collisionality [7] for ions

$$\nu_{*,i} \equiv \nu_{ii} / \nu_{i0} = \frac{\nu_{ii}}{\varepsilon^{3/2} V_{Ti} / qR}\ , \text{ where } \quad \nu_{i0} \equiv \frac{\varepsilon^{3/2} \cdot V_{Ti}}{q \cdot R}.\ , \quad V_{Ti} \equiv \sqrt{T_i / m_i} \tag{II.1}$$

and for electrons

$$\nu_{*,e} \equiv \nu_{ee} / \nu_{e0} = \frac{\nu_{ee}}{\varepsilon^{3/2} V_{Te} / qR}\ , \text{ where } \quad \nu_{e0} \equiv \frac{\varepsilon^{3/2} \cdot V_{Te}}{q \cdot R}., \quad V_{Te} \equiv \sqrt{T_e / m_e}\,. \tag{II.2}$$

Electron / ion gyroradius:

$$\rho_e = V_{Te}/\omega_{ce} = 2.38\cdot 10^2 T_e^{1/2} B^{-1}, \qquad \rho_i = V_{Ti}/\omega_{ci} = 1.02\cdot 10^4 T_i^{1/2} (BZ)^{-1}\sqrt{\mu} \qquad \text{(II. 3)}$$

Here $q(r)$ is the safety factor, ε is r/R and collisional frequencies ν_{ee} and ν_{ii} are given as

$$\nu_{ii} = \frac{4}{3}\sqrt{\pi} n_i Z_i^4 e^4 \ln\Lambda M_i^{-1/2} T_i^{-3/2} \quad \text{and} \quad \nu_{ee} = \nu_{ii}\sqrt{\frac{2M_i}{m_e}}\left(\frac{T_i}{T_e}\right)^{3/2} \qquad \text{(II.4)}$$

II. 1. Electron & ion particle flux.

$$\Gamma_i = \Gamma_e \qquad \text{(II.1.5)}$$

$$\Gamma_e = -\rho_e^2 \nu_{ei}\cdot q^2 \varepsilon^{-3/2} n_e \cdot K_{11}\cdot\left(1+\frac{T_i}{T_e}\right)\frac{\nabla n}{n} + \Gamma_{\nabla T_i} + \Gamma_{\nabla T_e} + \Gamma_{E_i} \qquad \text{(II.1.6)}$$

$$\Gamma_{\nabla T_i} = -\rho_e^2 \nu_{ei}\cdot q^2 \varepsilon^{-3/2} n_e \cdot K_{11}\cdot\left((1-A_i)\frac{T_i}{T_e}\right)\cdot\frac{\nabla T_i}{T_i} \qquad \text{(II.1.7)}$$

$$\Gamma_{\nabla T_e} = -\rho_e^2 \nu_{ei}\cdot q^2 \varepsilon^{-3/2} n_e \cdot\left(K_{12}-\frac{3}{2}K_{11}\right)\frac{\nabla T_e}{T_e} \qquad \text{(II.1.8)}$$

$$\Gamma_E = -K_{13}\cdot n_e \cdot \varepsilon^{-1/2} q\cdot c\cdot\frac{E_{//}}{B} \qquad \text{(II.1.9)}$$

And coefficients are given as follows:

$$K_{11} = 1.04\cdot\left\{\frac{1}{1+2.01\cdot\nu_{*,e}^{1/2}+1.53\cdot\nu_{*,e}} + \frac{1.414\cdot\varepsilon^3\cdot\nu_{*,e}}{1+0.89\cdot\nu_{*,e}\varepsilon^{3/2}}\right\} \qquad \text{(II.1.10)}$$

$$K_{12} = 1.2\cdot\left\{\frac{1}{1+0.76\cdot\nu_{*,e}^{1/2}+0.67\cdot\nu_{*,e}} + \frac{0.47\cdot\varepsilon^3\cdot\nu_{*,e}}{1+0.56\cdot\nu_{*,e}\varepsilon^{3/2}}\right\} \qquad \text{(II.1.11)}$$

$$K_{13} = 2.3\cdot\left\{\frac{1}{\left(1+1.02\cdot\nu_{*,e}^{1/2}+1.07\cdot\nu_{*,e}\right)\cdot\left(1+1.07\cdot\nu_{*,e}\cdot\varepsilon^{3/2}\right)}\right\} \qquad \text{(II.1.12)}$$

$$A_i = \frac{\left(1.17-0.35\cdot\nu_{*i}^{1/2}\right)-2.1\cdot\nu_{*i}^2\cdot\varepsilon^3\cdot\left(1+0.7\cdot\nu_{*i}^{1/2}\right)}{\left(1+0.7\cdot\nu_{*i}^{1/2}\right)\cdot\left(1+\nu_{*e}^2\cdot\varepsilon^3\right)\cdot\left(1+\nu_{*i}^2\cdot\varepsilon^3\right)} \qquad \text{(II.1.13)}$$

Here and below $E_{//}$ is the electric field along the magnetic field lines, which can be estimated as: $E_{//} \propto U/2\pi R$, where U is a toroidal loop voltage.

II. 2. Electron energy flux (heat flux and convective flux).

$$q_e + \frac{5}{2} T_e \cdot \Gamma_e = -\rho_e^2 \nu_{ee} \cdot q^2 \cdot \varepsilon^{-3/2} n_e \cdot T_e \cdot \left(K_{22} - \frac{3}{2} K_{12} \right) \frac{\nabla T_e}{T_e} + q_{e\nabla n} + q_{e\nabla Ti} + q_{eE} \tag{II.2.1}$$

$$q_{e\nabla n} = -\rho_e^2 \nu_{ee} \cdot q^2 \cdot \varepsilon^{-3/2} n_e \cdot T_e \cdot K_{12} \left(1 + \frac{T_i}{T_e} \right) \frac{\nabla n}{n} \tag{II.2.2}$$

$$q_{e\nabla T\,i} = -\rho_e^2 \nu_{ee} \cdot q^2 \cdot \varepsilon^{-3/2} n_e \cdot T_e \cdot K_{12} (1 - A_i) \frac{T_i}{T_e} \frac{\nabla T_i}{T_i} \tag{II.2.3}$$

$$q_{e\,E} = -K_{23} \cdot n_e \cdot T_e \cdot \varepsilon^{-1/2} \cdot q \cdot c \cdot \frac{E_{//}}{B} \tag{II.2.4}$$

Where:

$$K_{22} = 2.55 \cdot \left\{ \frac{1}{1 + 0.45 \cdot \nu_{*,e}^{1/2} + 0.43 \cdot \nu_{*,e}} + \frac{0.43 \cdot \varepsilon^3 \cdot \nu_{*,e}}{1 + 0.43 \cdot \nu_{*,e} \varepsilon^{3/2}} \right\} \tag{II.2.5}$$

$$K_{23} = 4.19 \cdot \left\{ \frac{1}{\left(1 + 0.57 \cdot \nu_{*,e}^{1/2} + 0.61 \cdot \nu_{*,e}\right) \cdot \left(1 + 0.61 \cdot \nu_{*,e} \varepsilon^{3/2}\right)} \right\} \tag{II.2.6}$$

II. 3. Ion energy flux.

$$\begin{aligned} & q_i + \frac{5}{2} \Gamma \cdot T_i = \\ & = -\rho_i^2 q^2 \cdot \nu_{ii} \cdot \left(K_i - \frac{5}{2} K_{11} \cdot \sqrt{\frac{m_e}{M_i}} \left((1 - A_i) \right) \cdot \right) \varepsilon^{-3/2} n \cdot T_i \cdot \frac{\nabla T_i}{T_i} + q_{i\nabla n} + q_{i\nabla Te} + q_{iE} \end{aligned} \tag{II.3. 1}$$

$$K_i \equiv 0.66 \cdot \left\{ \frac{1}{1 + 1.03 \cdot \nu_{*,i}^{1/2} + 0.31 \cdot \nu_{*,i}} + \frac{1.77 \cdot \varepsilon^3 \cdot \nu_{*,i}}{1 + 0.74 \cdot \nu_{*,i} \varepsilon^{3/2}} \right\} \tag{II.3.2}$$

$$q_{i\nabla n} = \rho_e^2 \nu_{ei} \cdot q^2 \varepsilon^{-3/2} n T_i \cdot \cdot K_{11} \left(A_i - \frac{5}{2} \right) \left(1 + \frac{T_i}{T_e} \right) \frac{\nabla n}{n} \tag{II.3.3}$$

$$q_{i\nabla T_e} = \left(A_i - \frac{5}{2} \right) \rho_e^2 \nu_{ei} \cdot q^2 \varepsilon^{-3/2} n_e \cdot T_i \cdot \left(K_{12} - \frac{3}{2} K_{11} \right) \frac{\nabla T_e}{T_e} \tag{II.3. 4}$$

$$q_{iE} = \left(A_i - \frac{5}{2} \right) K_{13} \cdot n_e \cdot T_i \cdot \varepsilon^{-1/2} q \cdot c \cdot \frac{E_{//}}{B} \tag{II.3.5}$$

$$E_{//} \approx U / 2\pi R \tag{II.3.6}$$

II. 4. Parallel current density.

$$J_{//} = -n_e T_e \cdot \varepsilon^{-3/2} q^2 \cdot \rho_e^2 \cdot \nu_e \{ K_{13} A_{1e} + K_{23} \nabla \ln T_e \} - \left(K_{33} \sqrt{\varepsilon} - 1 \right) \sigma_{//} U / 2\pi R \tag{II.4.1}$$

where

$$\sigma_{//} = \frac{n_e e^2 \tau_e}{m_e} \cdot \left(0.29 + \frac{0.46}{1.08 + Z} \right)^{-1} \tag{II.4.2}$$

and

$$A_{1e} = \left(1 + \frac{T_i}{T_e} \right) \frac{\nabla n}{n} + \left((1 - A_i) \frac{T_i}{T_e} \frac{\nabla T_i}{T_i} - \frac{3}{2} \frac{\nabla T_e}{T_e} \right) \tag{II.4.3}$$

$$A_i = \frac{\left(1.17 - 0.35 \cdot \nu_{*_i}^{1/2} \right) - 2.1 \cdot \nu_{*_i}^2 \cdot \varepsilon^3 \cdot \left(1 + 0.7 \cdot \nu_{*_i}^{1/2} \right)}{\left(1 + 0.7 \cdot \nu_{*_i}^{1/2} \right) \cdot \left(1 + \nu_{*_e}^2 \cdot \varepsilon^3 \right) \cdot \left(1 + \nu_{*_i}^2 \cdot \varepsilon^3 \right)} \tag{II.4.4}$$

$$K_{13} = 2.3 \cdot \left\{ \frac{1}{1 + 1.02 \cdot \nu_{*,e}^{1/2} + 1.07 \cdot \nu_{*,e}} + \frac{1}{1 + 1.07 \cdot \nu_{*,e} \varepsilon^{3/2}} \right\} \tag{II.4.5}$$

$$K_{23} = 4.19 \cdot \left\{ \frac{1}{\left(1 + 0.57 \cdot \nu_{*,e}^{1/2} + 0.61 \cdot \nu_{*,e} \right) \cdot \left(1 + 0.61 \cdot \nu_{*,e} \varepsilon^{3/2} \right)} \right\} \tag{II.4.6}$$

$$K_{33} = 1.83 \cdot \left\{ \frac{1}{1 + 0.68 \cdot \nu_{*,e}^{1/2} + 0.32 \cdot \nu_{*,e}} + \frac{1}{1 + 0.66 \cdot \nu_{*,e} \varepsilon^{3/2}} \right\} \tag{II.4.7}$$

II. 5. Bootstrap current density.

$$\frac{\partial \psi}{\partial t} = \frac{2\pi R}{\sigma_{//}} J_{//}, \qquad B_\theta = \frac{1}{2\pi R}\frac{\partial \psi}{\partial r}, \qquad q = \frac{r}{R}\cdot\frac{B}{B_\theta}, \quad s = \frac{r}{q}\cdot\frac{\partial q}{\partial r} \quad J_{BC} = \sqrt{\frac{2}{\varepsilon}}\frac{q\cdot p_e}{D(x)}\cdot F \qquad \text{(II.5.1)}$$

$$x = \sqrt{2\varepsilon}\ ,\ D(x) = 2.4 + 5.4\cdot x + 2.6\cdot x^2 \qquad \text{(II.5.2)}$$

$$F = c_1 \nabla \ln p_e + c_2 \nabla \ln p_i + c_3 \nabla \ln T_e + c_4 \nabla \ln T_i \qquad \text{(II.5.3)}$$

$$c_1 = \frac{4 + 2.6\cdot x}{\left(1 + 1.02\cdot\sqrt{\nu_{*e}} + 1.07\cdot\nu_{*e}\right)\left(1 + 1.07\cdot\varepsilon^{3/2}\cdot\nu_{*e}\right)}\ , \qquad c_2 = \frac{T_i}{T_e}c_1 \qquad \text{(II.5.4)}$$

$$c_3 = \frac{7.0 + 6.5\cdot x}{\left(1 + 0.57\cdot\sqrt{\nu_{*e}} + 0.61\cdot\nu_{*e}\right)\left(1 + 0.61\cdot\varepsilon^{3/2}\cdot\nu_{*e}\right)} - 2.5\cdot c_1 \qquad \text{(II.5.5)}$$

$$c_4 = \left(\frac{d + 0.35\cdot {\nu_{*i}}^{1/2}}{1 + 0.7\cdot {\nu_{*i}}^{1/2}} + 2.1\cdot\varepsilon^3\cdot {\nu_{*i}}^2\right)\frac{1}{\left(1 - \varepsilon^3\cdot {\nu_{*i}}^2\right)\left(1 + \varepsilon^3\cdot {\nu_{*e}}^2\right)}c_2 \qquad \text{(II.5.6)}$$

III. Turbulent transport model for bulk and pedestal region in TOKES

Anomalous transport models, employed in TOKES for bulk and pedestal regions based on giro-Bohm model of electrostatic micro-turbulence observed in large-scale tokamak plasmas. The turbulence reviles the onset threshold at some critical value of temperature gradient. For electrons we use a phenomenological model, described by Rebut-Lalia-Watkins, updated in comparison with experimental data **[**11**].** The turbulence in ions based on ion temperature gradient (ITG) transport, described by the gyro-Bohm IFS-PPPL model of Kotschenreuther et al. [8,9], where a parameterization of the critical gradient is obtained from a large number of linear gyro-kinetic simulations and with a smaller number of non-linear gyro-fluid simulations.

At the edge the dominant turbulence can be associate with the unstable Alfvén-drift waves which are appearing in finite β ($\beta \equiv nT / 8\pi B^2 \geq m_e / m_i$) plasmas, when the Alfvén wave couples to the drift wave [14]. The Alfvén drift turbulence suppression at the plasma edge is suggested as a triggering mechanism for the L to H transition. The stability theory of Alfvén drift-waves shows that with increasing plasma pressure the Alfvén waves get coupled to electron drift waves and as a consequence the unstable long wavelength perturbations (most important for transport) are suppressed. The instability can be characterised by two significant parameters, i.e. the normalised plasma beta, β_n , and the normalised collision frequency, ν_n . The suppression occurs when the normalised beta is greater than a critical value, i.e. $\beta_n > 1+\nu_n^{2/3}$, which depends on the normalised collision frequency ν_n . The Alfvén drift-wave model predicts the experimental trend of a roughly linear dependence of threshold temperature on magnetic field, with a weak dependence on density at high densities and a strong dependence on density at lower densities

We are considering to include in the near future the Alfvén-drift turbulence suppression as a trigger for the L to H transition in TOKES calculations.

As far as the radial transport in the SOL plasma concerns, we are employing there the Bohm diffusion coefficient, D_B , which can be taken either constant or as a function of electron temperature [15]:

$$D_B = cT_e / 16eB = D_0 \cdot T_e / B_T, \ m^2 / s \quad D_0 \equiv 6.25 \cdot 10^{-2} \qquad \text{(III.1)}$$

where B_T is the magnetic field in Tesla, temperature in eV.

The charts below present details of the RLW and ITG models, implemented in the TOKES.

III.1. Turbulence in electrons.

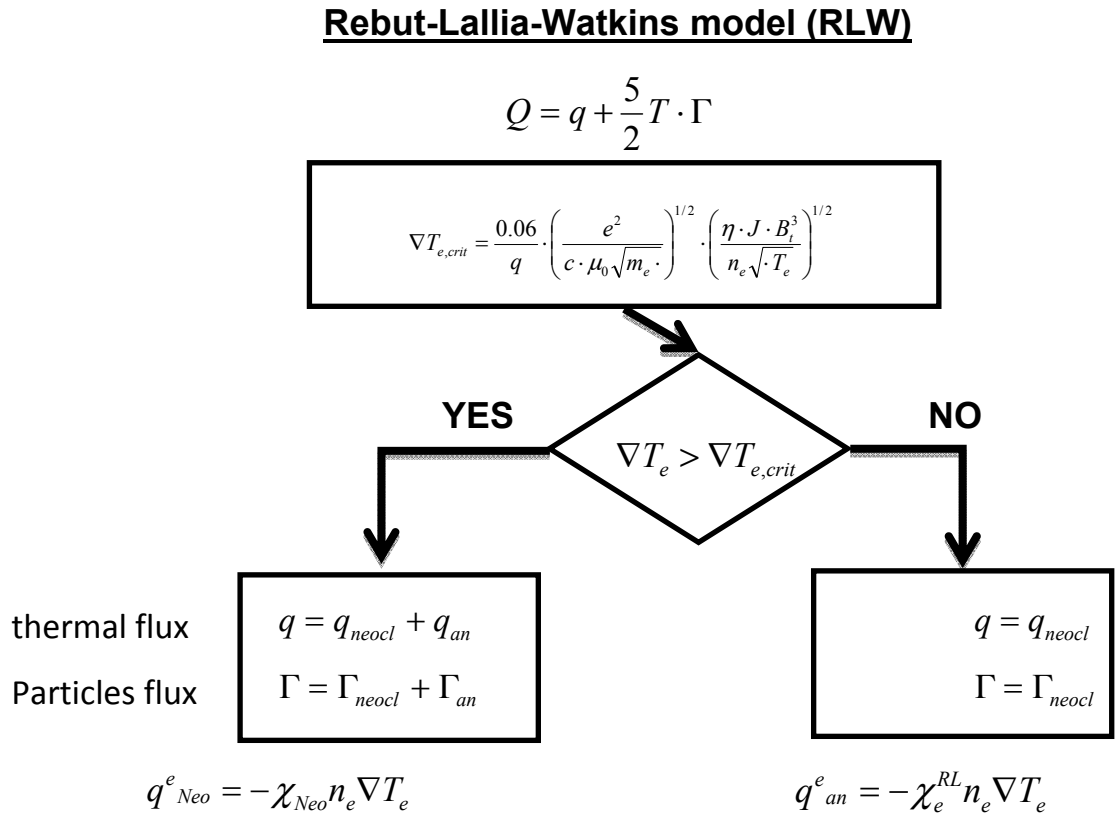

$$\chi_e^{RL} = \chi_{e0}^{RL} \cdot \left| \frac{\nabla T_e}{T_e} + 2 \frac{\nabla n_e}{n_e} \right| \cdot \frac{q^2}{\nabla q} \cdot \left(1 - \frac{\nabla T_{e,crit}}{\nabla T_e} \right) \cdot \theta[\nabla T_e - \nabla T_{crit}] \cdot \theta[\nabla q] \qquad \text{(III.1.1)}$$

where

$$\chi_{e0}^{RL} = 0.15 \cdot (\mu_0 m c^4)^{1/2} \frac{\left(1 - \sqrt{r/R}\right) \sqrt{\frac{T_e}{T_i}}}{B_t \sqrt{R}} \cdot \left(1 + Z_{eff}\right)^{1/2} \qquad \text{(III.1.2)}$$

Here $\mu_0 = 1/8\pi$, $\eta = 1/\sigma$ is the plasma resistivity, J is the plasma current, q is the safety factor.

III. 2. Turbulence in ions.

Ion Temperature Gradient model (ITG)

$$\eta_i \equiv \frac{\nabla T_i / T_i}{\nabla n_i / n_i} = \frac{L_{ni}}{L_{Ti}} \qquad \text{(III.2.1)}$$

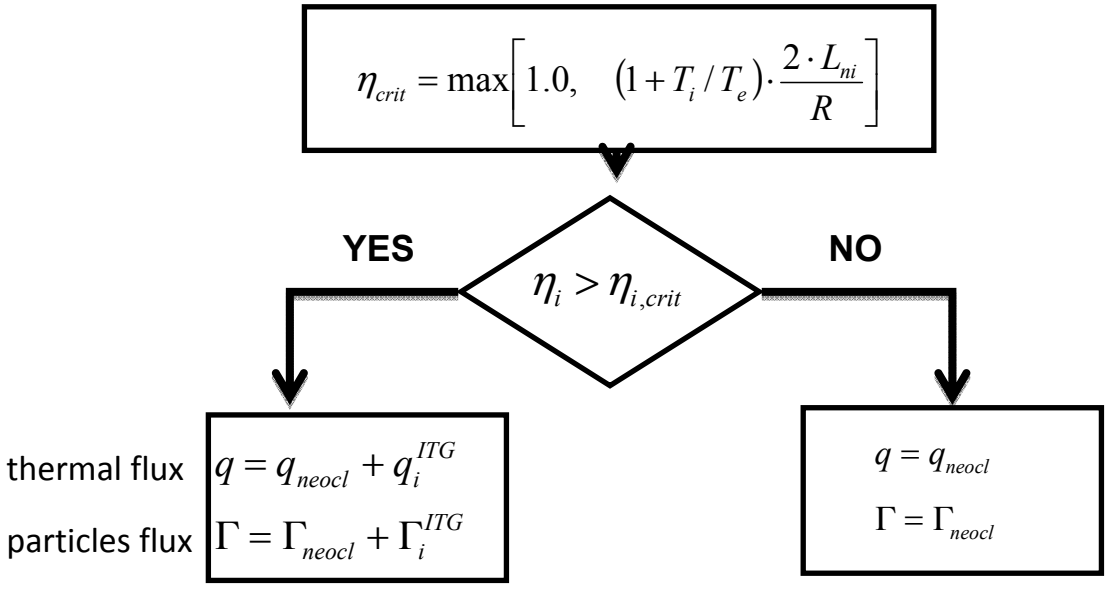

$$q_i^{ITG} = -\chi_i^{ITG} \cdot n_i \cdot \nabla T_i$$

$$D^{ITG} = -\, const.\chi_e^{ITG} \nabla n_e$$

$$\chi_i^{ITG} = \rho_i^2 \cdot \nu^{ITG}$$

where

$$\nu^{ITG} \equiv \frac{3}{2} \cdot \frac{1}{L_{ne}} \cdot \sqrt{\frac{2 \cdot T_e}{m_i}} \cdot (\eta_i - \eta_{crit}) \cdot (1 + 1/\eta_i) \cdot \theta(\eta_i - \eta_{crit}) \qquad \text{(III.2.2)}$$

IV. Model of the SOL/Divertor transport

IV. 1 Two dimensional fluid equations for SOL and divertor plasma in TOKES.

We are considering a 2D orthogonal coordinate system in the rectangular SOL domain with the *x*-axes across and the *y*-axes along the magnetic field lines (See Fig. 1). In tokamak configuration plasma near the wall has in general a complex curvilinear configuration. The magnetization of the plasma and relatively narrow boundary region, however, makes it possible to "straiten out" the separatrix and, in some approximation, to treat the problem in a rectangular geometry (Fig.1). If there is substantial uncertainty regarding the transport in radial direction, the effects of the curvature and of the variation of the poloidal magnetic field along B can be simply ignored. The SOL width, Δ_{sol}, is specified as a distance from the first wall to the separatrix and is much less than a minor radius, a .The plasma is assumed to be in steady state quite dense and cold (excluding transients), and is described by the system of hydrodynamic equations.

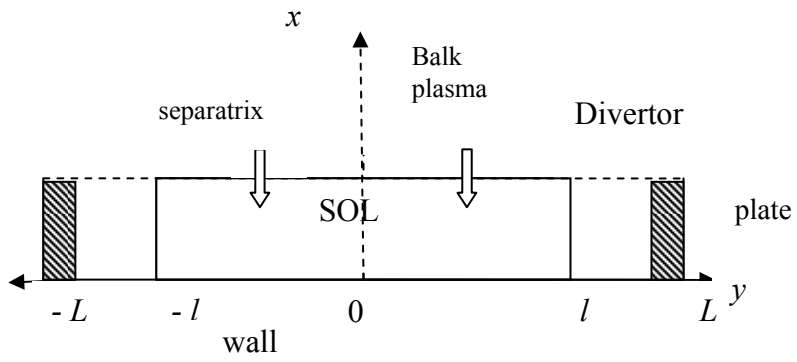

Fig. 1. The computational domain for the SOL and divertor region.

The following hydrodynamic equations for density, *n*, momentum, $P_{x,y} = m_i n V^{x,y}$ and energy in the SOL plasma are employed [15]:

$$\frac{\partial n}{\partial t} = \frac{\partial}{\partial x} n V_x - \frac{\partial}{\partial y}\left(n V_y\right) + nN\left\langle \sigma V \right\rangle_{ion} \qquad nV_x = -D_B(T)\frac{\partial n}{\partial x} \qquad \text{(IV. 1 .1)}$$

$$\frac{\partial nV_y}{\partial t}+\frac{\partial}{\partial y}\left(nV_yV_y\right)=-\frac{\partial 2nT}{m\partial y}-\frac{\partial}{\partial x}nV_yV_x+\frac{\partial}{\partial y}\left(\frac{\eta_{yy}}{m}\frac{\partial V_y}{\partial y}\right) \qquad \text{(IV. 1 .2)}$$

$$\frac{\partial}{\partial t}\left(3nT+\frac{mn\left(V_x^2+V_y^2\right)}{2}\right)+\frac{\partial}{\partial x}\left(5nT+\frac{mn\left(V_x^2+V_y^2\right)}{2}\right)V_x+$$
$$+\frac{\partial}{\partial y}\left(5nT+\frac{mn\left(V_x^2+V_y^2\right)}{2}\right)V_y+\frac{\partial}{\partial y}\chi^0T^{5/2}\frac{\partial T}{\partial y}+\frac{\partial}{\partial x}nD_BT\frac{\partial T}{\partial x}= \qquad \text{(IV. 1 .3)}$$

where

$$Q=-Q_{rad}-I_inN_0\left\langle\sigma V\right\rangle_{ion}-(\alpha_{rec}+n\beta_{rec})n^2 \qquad \text{(IV. 1 .4)}$$

Here $T\equiv T_e=T_i$, η_{yy} is the viscosity and χ^0 is the Spitzer-Harm conductivity coefficients along B (for one eV), D_B is the radial diffusion coefficient taken in the SOL as 1m^2/sec. Generalization to functional Bohm coefficient is straightforward. Particle source, $nN\left\langle\sigma V\right\rangle_{ion}$ and energy sink, Q, due to radiation, ionization and recombination of neutrals N_0 which are currently modelled by specifying arbitrary the distribution of neutral atoms in divertor.

The ionization $\left\langle\sigma V\right\rangle_{ion}$, the radiative, α_{rec}, and the three body recombination, β_{rec}, the charge exchange collision, $\tau_{cx}=1/N_0\left\langle\sigma_{cx}V_i\right\rangle$, and the radiation equilibrium for cold neutrals, Q_{rad}, (for of zero temperature and zero velocity) are employed:

$$\frac{\partial n}{\partial t}=n_e\left[S_0N_0-\alpha_rn_i-\alpha_3n_in_e\right] \qquad \text{(IV. 1 .5)}$$

$$3\frac{\partial n_iT}{\partial t}+\ldots=n_e\left[-I_1S_0N_0-3T\alpha_rn_i-\frac{3}{2}T\alpha_3n_in_e\right]-Q_{rad}-\left(\frac{3}{2}T+\frac{m_iV_y^2}{2}\right)\frac{n_i}{\tau_{cx}} \qquad \text{(IV. 1 .6)}$$

$$Q_{rad}=I_1\alpha_rn_in_e+n_zn_eL_z+N_0n_eL_H \qquad \text{(IV. 1 .7)}$$

$$\frac{\partial n_iV_y}{\partial t}=-n_e\left[\alpha_rn_i+\alpha_3n_in_e\right]V_y-\frac{n_iV_y}{\tau_{cx}} \qquad \text{(IV. 1 .8)}$$

Here n_z is the impurity concentration and L_z is the cooling rate for impurity radiation.

The following improvements are foreseen in near future:

1) separation of electron and ion temperatures, $T_e\neq T_i$,

2) appropriate model of the neutral atoms (self-consistent calculation),

3) equations for realistic curvilinear geometry.

4) the terms with parallel current along the magnetic field lines will be added

IV. 2. Boundary conditions. The 2D fluid equations are required initial and boundary conditions at the computation boundaries. As initial conditions, density, temperature and velocities are taken from the 1D analytical profiles along the B and exponential across the SOL. Since we are looking for stationary solution, this choice is unimportant. The kinetic effects in boundary conditions are neglected and all transmission coefficients derived assuming a half Maxwellian function for the incident particles. We also neglect here the influence of impurities on the boundary parameters. One can distinguish five boundaries: at the separatrix, in private zone region, at the divertor plates and at the first wall.
Input particles, Γ and heat, $Q_e = Q_i = Q$ fluxs are specified at the separatrix:

- **Separatrix between the SOL and core:** $x = 1 \;\; (r = \Delta_{sol}), \quad -l \le y \le l$

$$q_x = -nD_B \left.\frac{\partial T}{\partial x}\right|_{x=1;\,-d\le y\le d} = Q / S_{sep} \qquad \text{(IV.2.2)}$$

$$nV_x = -D_B \left.\frac{\partial n}{\partial x}\right|_{x=1;\,-d\le y\le d} = \Gamma / S_{sep} \qquad \text{(IV.2.2)}$$

- **Divertor & privat zone boundary:** $x = 1 \;\; (r = \Delta_{sol}), \quad |d| \le y \le |L|$**)**

$$q_x = -nD_B \left.\frac{\partial T}{\partial x}\right|_{x=1;\,|d|\le y\le |L|} = 2nv_T T \qquad \text{(IV.2.3)}$$

$$nV_x = -D_B \left.\frac{\partial n}{\partial x}\right|_{x=1;\,|d|\le y\le |L|_y} = \frac{1}{4} v_T n \qquad \text{(IV.2.4)}$$

- **Divertor plates:** $y = \pm L \quad 0 \le x \le 1$

$$q_s = 2nT \cdot c_s(T) \qquad \text{(IV.2.5)}$$

$$V_s = c_s(T), \quad T = T_w \qquad \text{(IV.2.6)}$$

where T_w is the wall temperature, $c_s(T)$ is the sound speed.

- **Private region:** $x = 1 \quad -L \le y \le -d; \;\; d \le y \le L$

$$q_s = 2(1-\alpha) nT \cdot c_s(T) \qquad \text{(IV.2.7)}$$

$$nV_s = \frac{1}{4}(1-\alpha) n \cdot c_s(T)$$

where α is some reflexion coefficient $\cong 2$, which describes the ratio of reflected back from privat region particles.

- **Wall:** $x = 0,\ -L \le y \le +L$

We assume $n = 0 \quad T = 0$ (IV.2.8)

The boundary conditions at the divertor plate can be generalized by assuming that the distribution function at the boundary is a one directed shifted Maxwellian for ions due to the acceleration in the electric pre-sheath, $e\varphi$, and truncated at some velocity double side Maxwellian for electrons, because of cut-off in the retarding electric field. The boundary conditions at the plate then can be obtained by equating the fluid particle and energy fluxes to kinetic ones:

$$(\frac{5}{2} n V_s T_e + q_e) = f_e T_e n V_{Te} \tag{IV.2.9}$$

$$(\frac{m_i V_i^2}{2} + \frac{5}{2} T_i) n V_i + q_e = f_i T_i n V_{Ti} \tag{IV.2.10}$$

$$(m_i n V_i^2 + n T_i + n T_e - \eta_i \frac{\partial V_i}{\partial y}) = f_{pe} T_e n + f_{pi} T_i n \tag{IV.2.11}$$

where

$$f_e = 2 + \varepsilon \tag{IV.2.12}$$

$$f_i = \frac{e^{-M_1^2}(2 + M_1^2) - \sqrt{\pi} M_1 \left(M_1^2 + \frac{1}{2} \right) Erf(-M_1)}{G(M_1)} \cdot \tag{IV.2.13}$$

$$f_{pi} = \frac{2\sqrt{\pi} M}{G(M_1)} \cdot \left\{ \frac{M_1}{\sqrt{\pi}} e^{-M_1^2} + (M_1^2 + \frac{1}{2}) Erf(-M_1) \right\} \tag{IV.2.14}$$

$$f_{pe} = \frac{2\sqrt{\pi} M}{G(M_1)} \cdot \left\{ -\sqrt{\frac{\varepsilon}{\pi}} e^{-\varepsilon} + \frac{1}{2} Erf(-\varepsilon) \right\} \tag{IV.2.15}$$

Here $M = V_i / V_{Ti}$ where V_i is the fluid velocity along B at the plate and V_{Ti} is the ion thermal velocity; $Erf(x) = \frac{2}{\sqrt{\pi}} \int_{-\infty}^{x} e^{-t^2} dt$. The parameter M_1 is equal to M if $V_i \geq C_s$, while at $V_i \leq C_s$, it is found from the condition $\int_0^{\infty} F_i(M_1) V dV / \int_0^{\infty} F_i(M_1) dV = C_s$, where F_i is boundary distribution function for ions, $F(M_1)_i = \frac{c_i \vartheta(u)}{\sqrt{\pi V_{Ti}}} \exp\{-(u - M_1)^2\}$, $u \equiv V / V_{Ti}$, $\vartheta(x)$ is the Heaviside function and $C_s = \sqrt{5(T_e + T_i)/3m_i}$ is the sound velocity. The dimensional potential of the sheath $\varepsilon = e\varphi / T_e$ is found from quasineutrality condition [19]:

$$\varepsilon = \frac{\ln \sqrt{\frac{m_i}{m_e} \frac{T_e}{T_i}} Erf(-M_1)}{G(M_1) Erf\left(-\sqrt{\varepsilon}\right)} \qquad \text{(IV.2.16)}$$

where $G(M_1) \equiv e^{-M_1^2} + \sqrt{\pi} M_1 Erf(-M_1)$

Note that the plasma parameters may have a discontinuity at the boundary, but the fluxes remain continuous.

The value of the electric potential in pure plasma at the plate is about $e\varphi \propto 3.5 \cdot T_e$ in absence of current flow to the plate and electron emission. But this potential can considerable increase in non stationary case, when the material surface becomes due to erosion not even.

IV. 3 **Kinetic effects in the SOL plasma.** One of the factors limiting the applicability of the hydrodynamic approach is the effect of the suprathermal particles upon the parallel heat conductivity and viscosity. Even when the conditions of hydrodynamics are strongly satisfied (e.g. the mean free path of particles are small compare with the SOL length), the expressions for the parallel heat conduction and viscosity coefficients turn out to be wrong. This is related to the fact that hydrodynamic fluxes are higher order moments and are determined mainly by suprathermal particles for which the hydrodynamic approximation turns out to be violated. When this occurs, the heat and momentum fluxes become non-local in their nature. It is shown [19] that the non-local representation for fluxes naturally follows from the equations for higher order moments of the distribution function, provided that the spatial derivatives of these moments with respect to coordinates are retained. This allows one to use differential equations for moments and their derivatives instead of complicated integral expressions for the flux in numerical calculations. In simulation of kinetic effects a simplified approach is often used, assuming the heat flux to be constrained from above by the quantity

$$q_e = \frac{q_{SH} \cdot q_{kin}}{q_{SH} + q_{kin}}, \qquad \text{(IV. 3.1)}$$

where $q_{kin} = FLF \cdot 2nTV_{Te}$. Here FLF = 0.1-0.3 is a flux limiting factor which is found either from experiments or from the results of numerical solution of a kinetic equation [20-22]. Unfortunately, the great uncertainty found in the experimental data does not allow one to make a quantitative conclusion about the value of FLF. As a non-local approach, FLF increases the upstream plasma temperature and reduces the density, whilst not changing significantly the plasma parameters in the vicinity of the plate. However, with the introduction of the FLF the transport remains local. Such an approach does not represent all the features related to the nature of the non-local transport. Furthermore, the applicability of the integral expression is limited to cases with low parallel plasma gradient, where a strong anisotropy in the particle distribution function can be neglected. In cases of large temperature gradient the main contribution to transport is supplied by the "tail" particles. These hot electrons can reach the divertor plate and, essentially produces an increase in the sheath potential (see Fig. 2) that can result in increased plate erosion. For a higher sheath potential, however, the energy transfer ability of each electron-ion pair on the plate is increased. The implication is, that the plasma temperature near the plate may be less than that predicted by fluid modelling, thus reducing sputtering by hot ions to some extent. In summary of the above arguments, one can say that the non-local transport redistributes the fluxes over the thermal layer, reducing the peak power load. Therefore existing hydrodynamic models probably give pessimistic values of heat loading and local plasma temperature at the divertor plate. The kinetic effects can noticeably affect the transport of impurities in the divertor, in particular that of helium. The localisation of impurities is determined by the competition of many forces, including the ion thermal force. Under ITER divertor plasma conditions one can expect a reduction in the ion thermal force in comparison with the hydrodynamic limit [16,17]. In the case of helium ions this reduction is approximately equivalent to a reduction of the thermal force coefficient by a factor of two to three.

Summarize, we are suggesting the following kinetic correction in fluid equation. Since electrons are predominantly deviate from hydrodynamic limit the local expression for parallel heat conductivity in energy equation, $q_{e,SH}(y) = -\chi_{SH}\partial T_e / \partial y$ can be replaced by:

$$q_e(y) = \int_{-L}^{+L} G(y - y') \cdot q_{e,SH}(y')dy', \qquad \text{(IV. 3.2)}$$

where

$$G(y-y') \approx \frac{1}{2\lambda(y')} \exp\left(-\left| \int_{y}^{y'} \frac{d\eta}{\lambda(\eta)} \right| \right) \qquad \text{(IV. 3.3)}$$

Here

$\lambda(y) = V_{Te}(T_e^*) \cdot \tau_{ei}(n, T_e^*)$ and $T_e^* \approx 3.8 \cdot T_e$ [19]

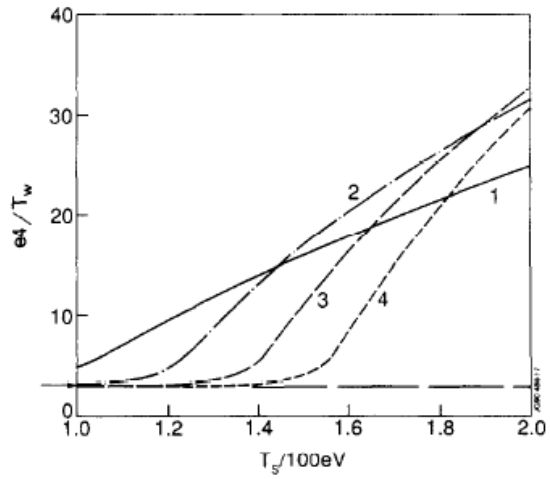

Fig. 2. *The influence of hot particles on the sheath potential* $e\varphi / T_w$ *versus temperature* T_s*, and density* n_s *at the separatrix: (1)* $n_s = 1 \cdot 10^{13} cm^{-3}$*, (2)* $n_s = 2 \cdot 10^{13} cm^{-3}$*,(3)* $n_s = 3 \cdot 10^{13} cm^{-3}$*,(4)* $n_s = 4 \cdot 10^{13} cm^{-3}$ *and* T_w *is, the temperature at the plate.*

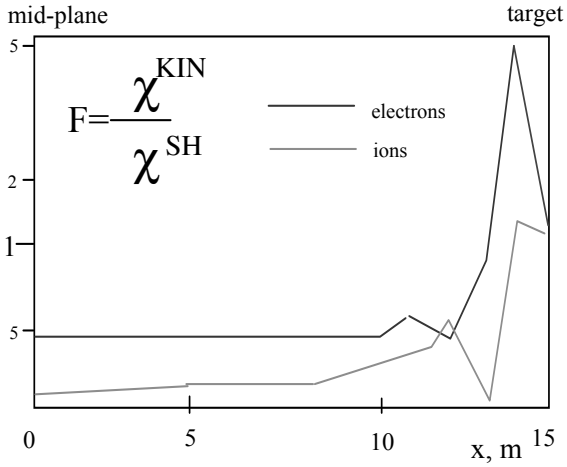

Fig. 3 *Kinetic correction to heat conductivity vs distance along B; here* $F = 1/FLF$ *; Heat flux near the plate increases several times due to the contribution of suprathrmal particles* [22]

Analyse of kinetic correction of fluid equations shows, that the suprathermal particles are largely responsible for the parallel transport in boundary plasma. Non-locality produces two kinds of effect on the heat flow: reduction in the hot region of the SOL and enhancement in the cool region near the plate. Reduction of the heat conductivity results in stronger temperature gradients and, this, in combination with pressure balance along B reduces upstream plasma densities. Suprathermal particles can considerable enhance the sheath potential and increase neutral ionization and excitation rates. An efficient numerical procedure for kinetic correction to 2D fluid includes the following corrections:

1) the flux limit factors for electron and ion heat flux along B or

2) the introduction of non-local heat flux expression (which changes energy equation to integer-differential and requires another numerical solver).

IV. 4 Electric field and hot spots formation on the divertor plates.

Intensive erosion leads to a formation of corrugate wedge-type shape of W-brush tungsten target [23-25] (Fig.6). We consider here a sheath region bounded by a corrugated surface of divertor plate and a flat boundary held to a constant voltage bias. The rough

surface influences the equipotential lines next to surface and can considerable enhance erosion due to the electric arcs initiation. These arcs, triggered by abnormal electric field at wedge-like edges of the tungsten divertor plates, could be an additional source of impurities and dust.

Analysis of the surface roughness shows that topography of the material surface after exposition has a shape of sharp granules with the pronounced wedge-type shape of 1-3mm in height and width. The sharpening of surface roughness changes the electric field pattern in adjacent plasma by increasing the electric field at the vicinity of the wedge tips. As it is shown further the enhanced electric field could trigger arcs and initiate hot spots. We evaluate the electric potential φ / T in the region by solving the 2D Poisson equation at the plate:

$$\frac{\partial^2 \varphi}{\partial x^2} + \frac{\partial^2 \varphi}{\partial y} = \frac{4\pi j_i \sin\phi}{V_{th} T} (1 - \sqrt{m_i / 2\pi m_e} e^{-e\varphi / T}) \approx \varphi / \lambda_d^2 , \qquad \text{(IV. 4.1)}$$

where λ_d is the Debye length, V_{th} is the ion thermal velocity, ϕ is the angle between magnetic field and the plate, j_i. is the ion saturation current. Here x is the coordinate along the plate and y is along the magnetic field line. The boundary values at the conductor ($\varphi = 0$) and in the opposite boundary ($\varphi = 1$) was assumed. The standard variation formulation of a finite element method can be used to solve the problem [27]. The potential at the lateral magnetic field lines bounded the SOL domain, was specified as a linear function of y. Numerical grids are shown on the Figs. 4 and 8.

After integration of Eq. IV. 4.1 one can obtain a set of equipotential lines by the numerical spline interpolation. The roughness of the equipotential lines is gradually changed toward the top region, where $\varphi \sim 1$ is assumed. First, a sinusoid-type surface shape was taken to check the calculation accuracy. Fig. 4 and Fig. 5 show the greed's pattern and resulting equipotential lines above the sinusoidal corrugated surface of divertor plate.

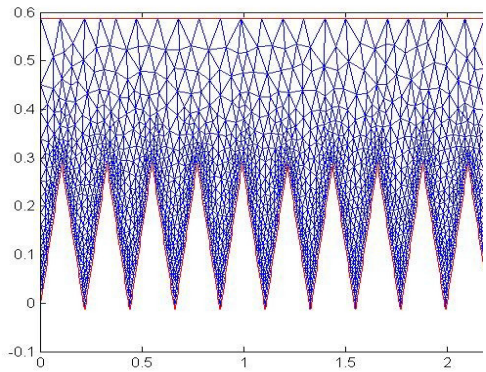

Fig. 4 *Numerical grids for Eq. 1. A sinusoidal corrugated surface of divertor*

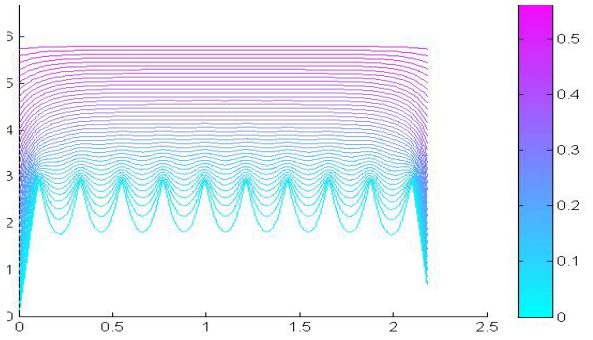

Fig. 5 *Contours of electric potentials above the sinusoidal corrugated surface of divertor*

plate.

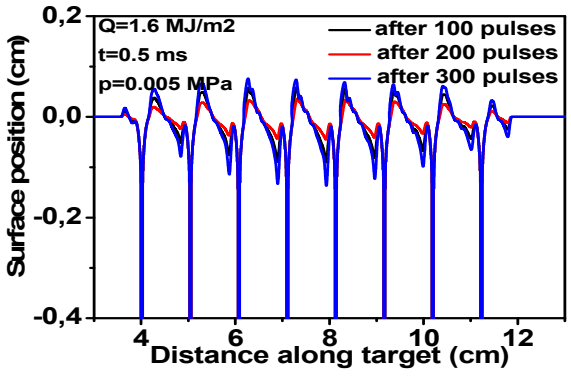

Fig.6 *View of W-brush target corrugated under repetitive ELM-like plasma heat loads. Q = 1.6 MJ/m^2, τ =0.5 ms* [24]

plate shown before;

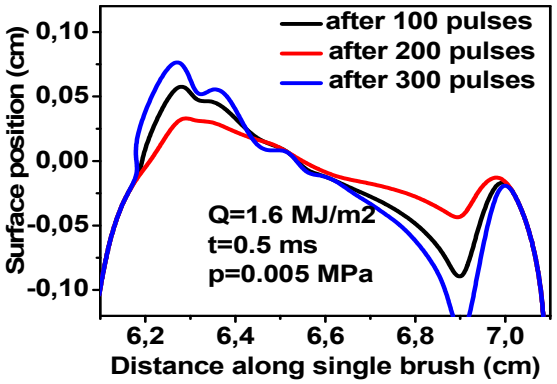

Fig. 7 *View of a single W-brash after melting and splashing the molten layer after different numbers of pulses* [24].

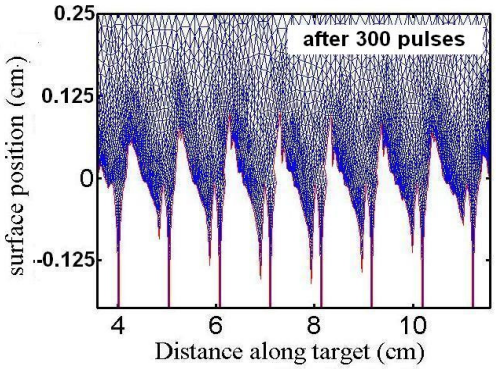

Fig. 8 *Numerical grid for Eq. 1. Corrugated brash type divertor plate after 300 ELMs pulses* [28].

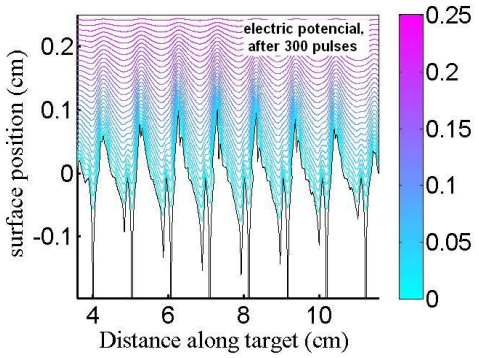

Fig. 9 *Contours of equipotential lines, graduated as shown on the right hand side of the picture.*

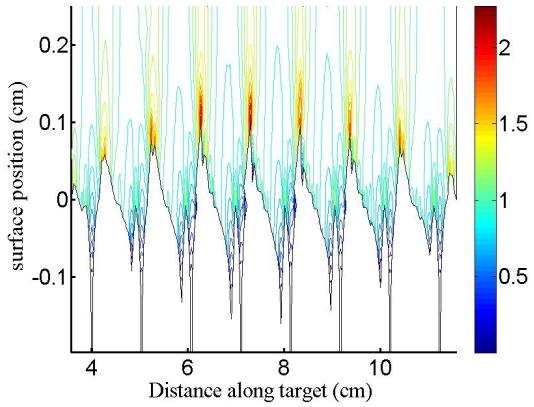

Fig. 10 *Electric field lines graduated in right column.*

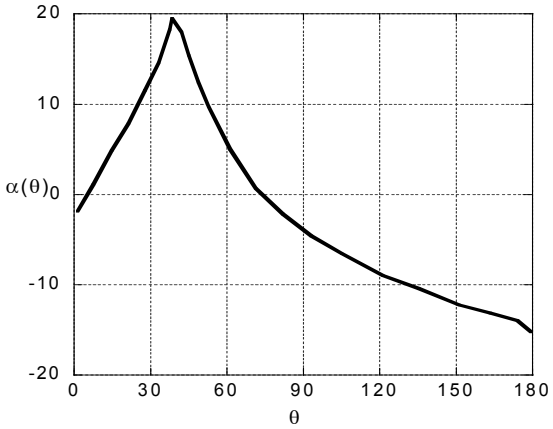

Fig. 11 α *values vs wedge cone angle* θ *.* $E_r \sim 1/r^{\alpha}$, $\alpha < 0$ [28]

One can see that at the wedge tips the electric field can be so strong, that can easily facilitate the generation of arcs and hot spots. Electric field on perfect metallic wedges behaves like $E_r \sim r^{\alpha}$, presenting a singularity when $\alpha < 0$ [28]. Abnormal electric field appears usually for very sharp wedges, $\alpha \approx -\frac{1}{4}\theta^2 + O(\theta)$. This can be found analytically by solving Laplace's equation in spherical coordinate system for 2D wedge shape. A quasi-analytic procedure based on the theory of Legendre and Lame's functions was used to determine α. Formation of the hot spots requires the current density on the surface in excess to some threshold value ~ 0.1-1A/cm^2 (for W). This can be expected first from the wedge tips at some cone angle value (see Fig.6,7), when a strong increase of the field emission of electrons takes place. The current density of electrons emission is described by the Fawler-Nordheim tunnelling law and strongly depends on the electric field. At the electric field value $E \sim 3 \cdot 10^7 V/cm$ the field emission current reaches the threshold value $\sim 1 A/cm^2$ and triggers the hot spots. The electric field at the wedge tip can be estimated as $E_0 / E \sim (r/a)^{\alpha(\theta)}$, where $E_0 \sim 1keV$ is the energy of incident particles, $a \sim 1cm$ is the typical width of the wedge (see Fig. 6) and $\alpha(\theta)$ is the function of the wedge cone angle θ (see Figs. 10,11). This allows one to estimate the critical value of the wedge curvature (radius) at the tip position. Estimation gives, $r \sim 0.5cm$, which is in the range of expected values (see Fig. 11). This evaluation indicates the high probability of the hot spot formation and arcs initiation on the diverter plates caused by surface distraction during the multiple transient events. This additional erosion mechanism could lead to substantial contamination of plasma and the material distraction and requires a further investigation.

V. Numerical approach. Application of the modified Belocerkovsky procedure to the SOL equations.

The system of 2D fluid equations (1,2,3) is solved by using the ‘‘split step’’ method both for different special directions and for different physics processes as well [29,30]. For the later one we are employing the Belocerkovsky numerical procedure, which consist of three sub-steps [31]. Below we will consider $T_e \neq T_i$ and will dill with the following set of transport equation:

$$\frac{\partial n}{\partial t} + \frac{\partial}{\partial x}\left(nV^x\right) + \frac{\partial}{\partial y}\left(nV^y\right) = n\left[S_0 n_0 - \alpha_{rec} n - \alpha_3 n^2\right] \equiv n\left(\gamma_{ion} - \gamma_{rec}\right), \qquad \text{(V.1)}$$

where

$$\gamma_{ion} = S_0 n_0 \qquad \gamma_{rec}(n) = -n\left[\alpha_{rec} + \alpha_3 n\right] \tag{V.2}$$

$$\frac{\partial nV^y}{\partial t} + \frac{\partial}{\partial y}\left(nV^y V^y\right) + \frac{\partial}{\partial x} nV^y V^x = -\frac{\partial n\left(T_e + T_i\right)}{m_i \partial y} + \frac{\partial}{\partial y}\left(\frac{\eta_{yy}}{m_i}\frac{\partial V^y}{\partial y}\right) - \\ - n\gamma_{rec}(n)V_y - \frac{nV_y}{\tau_{cx}} \tag{V.3}$$

$$nV^x = -D_\perp \frac{\partial n}{\partial x} \tag{V.4}$$

$$\frac{\partial}{\partial t}\left(\frac{3}{2}\left(T_e + T_i\right) + \frac{m_i\left(V_y^2 + V_x^2\right)}{2}\right)n + \frac{\partial}{\partial x}\left(\frac{5}{2}\left(T_e + T_i\right) + \frac{m_i\left(V_y^2 + V_x^2\right)}{2}\right)nV_x + \\ \frac{\partial}{\partial y}\left(\frac{5}{2}\left(T_e + T_i\right) + \frac{m_i\left(V_y^2 + V_x^2\right)}{2}\right)nV_y + \frac{\partial}{\partial y}\chi_e T_e^{5/2}\frac{\partial T_e}{\partial y} + \frac{\partial}{\partial x} nD_\perp^e \frac{\partial T_e}{\partial x} + \\ + \frac{\partial}{\partial y}\chi_i T_i^{5/2}\frac{\partial T_i}{\partial y} + \frac{\partial}{\partial x} nD_\perp^i T_i \frac{\partial T_i}{\partial x} = -Q_{rad} - \left(\frac{3}{2}T_i + \frac{m_i\left(V_y^2 + V_x^2\right)}{2}\right)\frac{n_i}{\tau_{cx}} + \\ - I_1 n\gamma_i - \frac{3}{2}\left(T_e + T_i + \frac{m_i\left(V_y^2 + V_x^2\right)}{2}\right)n\gamma_r \tag{V.5}$$

$$\frac{\partial}{\partial t}\left(\frac{3}{2}nT_e\right) + \frac{\partial}{\partial x}\left(\frac{5}{2}nT\right)V_x + \frac{\partial}{\partial y}\left(\frac{5}{2}nT_e\right)V_y = V_x\frac{\partial nT_e}{\partial x} + V_y\frac{\partial nT_e}{\partial y} + \frac{3m_e}{m_i}n\frac{T_i - T_e}{\tau_{ei}} + \\ \frac{\partial}{\partial y}\chi_t T_e^{5/2}\frac{\partial T_e}{\partial y} + \frac{\partial}{\partial x} nD_\perp^e \frac{\partial T_e}{\partial x} \tag{V.6}$$

First we will employ the velocity-pressure solver together with energy equations (**the Lagrange sub-step**):

$$nV_x = -D_\perp(T)\frac{\partial n}{\partial x} \tag{V.7}$$

$$\frac{\partial nV^y}{\partial t} = -\frac{\partial n\left(T_e + T_i\right)}{m\partial y} + \frac{\partial}{\partial y}\left(\frac{\eta_{yy}}{m}\frac{\partial V^y}{\partial y}\right) \tag{V.8}$$

$$\frac{\partial}{\partial t}\left(\frac{3}{2}n\left(T_e + T_i\right) + \frac{mn\left(V_y^2 + V_x^2\right)}{2}\right) = \frac{\partial}{\partial x}\left(n\left(T_e + T_i\right)V_x\right)V + \frac{\partial}{\partial y}\left(n\left(T_e + T_i\right)V_y\right) \tag{V.9}$$

where the new velocities are found as a function of density and temperature, taken from the previous time step, η_{yy} is the parallel viscosity. The discretization for *x*-diffusion (implicit scheme) results is:

$$\frac{\tilde{n}_{ij} - n_{ij}}{\Delta t} = \frac{\partial}{\partial x} D_{\perp} \frac{\partial \tilde{n}_{ij}}{\partial x}, \tag{V.10}$$

then using $\tilde{n}_{ij}$ and n_{ij} one can calculate the total number of particles, crossing the cell boundary

$$dN^{x}_{i+1/2\,j} = n_{ij} \tilde{V}^{x}_{i+1/2\,j} S^{along}_{i+1/2\,j} \tag{V.11}$$

$$dN^{x}_{H_x j} = -D_{\perp} \frac{\tilde{n}_{ij} - \tilde{n}_{ij}}{\Delta x} S^{along}_{H_x j} = \Gamma_{H_x j} \tag{V.12}$$

$$dN^{x}_{ij} = \left(\tilde{n}_{ij+1} - n_{ij+1}\right) V^{cell}_{ij} + dN^{x}_{ij+1}, \quad i = \left(H_x - 1\right)...1 \tag{V.13}$$

The explicit formula for *y*-convection reads as:

$$\tilde{V}^{y}_{ij} = V^{y}_{ij} - \frac{\Delta t}{m_i N_{ij}} \left(\left(p_{ij+1} + p_{ij}\right) S_{j+1/2} - \left(p_{ij-1} + p_{ij}\right) S_{j-1/2}\right) \tag{V.14}$$

$$\tilde{V}^{y}_{ij+1/2} = \frac{\left(\tilde{V}^{y}_{ij} + \tilde{V}^{y}_{ij+1}\right)}{2} \tag{V.15}$$

With total plasma particles number $N_{ij} = n_{ij} V^{cell}_{ij}$ in the cell *ij*, the plasma pressure $p_{ij} = n\left(T_e + T_i\right)_{ij}$, the ion thermal energy density $e_{e;ij} = \frac{3}{2} n T_{e;ij}$, and the total energy density

$$e_{ij} = \left(\frac{3}{2} n\left(T_e + T_i\right) + \frac{m_i \left(V_y^2 + V_x^2\right) n}{2}\right)_{ij}. \tag{V.16}$$

The total energy change at the Lagrange sub-step is:

$$\widetilde{E}_{ij} = E_{ij} - \frac{\Delta t}{mN_{ij}}\left(p_{ij+1/2}V^{y}_{i,j+1/2}S^{cross}_{ij+1/2} - p_{ij-1/2}V^{y}_{i,j-1/2}S^{cross}_{ij-1/2}\right) - \frac{\Delta t}{m}\left(p_{i+1/2,j}V^{x}_{i+1/2,j}S^{along}_{i+1/2\,j} - p_{i-1/2,j}V^{x}_{i-1/2,j}S^{along}_{i-1/2\,j}\right) \tag{V.17}$$

$$\widetilde{E}_{e,ij} = E_{e,ij} + \frac{\Delta t}{m}\left(V^{y}_{i,j}\frac{\left(p^{e}_{ij+1/2} - p^{e}_{ij-1/2}\right)}{\Delta y_{ij}} + V^{x}_{i,j}\frac{\left(p^{e}_{i+1/2\,j} - p^{e}_{i-1/2\,j}\right)}{\Delta x_{ij}}\right)V^{cell}_{ij} =$$

$$= E_{e,ij} + \frac{\Delta t}{m}\left(V^{y}_{i,j}\left(p^{e}_{ij+1/2} - p^{e}_{ij-1/2}\right)S^{cross}_{i+1/2\,j} + V^{x}_{i,j}\left(p^{e}_{i+1/2\,j} - p^{e}_{i-1/2\,j}\right)S^{along}_{i+1/2\,j}\right) \tag{V.18}$$

In the following sub-step we will use the definition, which depends on sign of velocity:

$$dN^{y}_{j+1/2} = n_{j\pm1}\widetilde{V}^{y}_{ij+1/2}S^{cross}_{j+1/2} \text{ with } n_{j\pm1} = \begin{cases} n_{j-1}, \text{ if } \widetilde{V}^{y}_{ij-1/2} > 0 \\ n_{j}, \text{ if } \widetilde{V}^{y}_{ij-1/2} \le 0 \end{cases} \tag{V.19}$$

In the second (Euler) sub-step we are solving the system of equations:

$$\frac{\partial n}{\partial t} + \frac{\partial}{\partial x}\left(nV^{x}\right) + \frac{\partial}{\partial y}\left(nV^{y}\right) = n\left(\gamma_{ion} - \gamma_{rec}(n)\right) \tag{V.20}$$

$$\frac{\partial nV^{y}}{\partial t} + \frac{\partial}{\partial y}\left(nV^{y}V^{y}\right) + \frac{\partial}{\partial x}\left(nV^{y}V^{x}\right) = 0 \tag{V.21}$$

$$\frac{\partial nV^{x}}{\partial t} + \frac{\partial}{\partial x}\left(nV^{x}V^{x}\right) + \frac{\partial}{\partial y}\left(nV^{x}V^{y}\right) = 0 \tag{V.22}$$

$$\frac{\partial}{\partial t}\left(\frac{3}{2}\left(T_e + T_i\right) + \frac{m_i\left(V_y^2 + V_x^2\right)}{2}\right)n + \frac{\partial}{\partial x}\left(\frac{3}{2}\left(T_e + T_i\right) + \frac{m_i\left(V_y^2 + V_x^2\right)}{2}\right)nV_x + \frac{\partial}{\partial y}\left(\frac{3}{2}\left(T_e + T_i\right) + \frac{m_i\left(V_y^2 + V_x^2\right)}{2}\right)nV_y = -Q \tag{V.23}$$

$$\frac{\partial}{\partial t}\left(\frac{3}{2}nT_e\right) + \frac{\partial}{\partial x}\left(\frac{3}{2}nT_e\right)V_x + \frac{\partial}{\partial y}\left(\frac{3}{2}nT_e\right)V_y = -I_1 n\gamma_i - \frac{3}{2}T_e n\gamma_r \tag{V.24}$$

Here

$$Q \equiv \left(\frac{3}{2} T_i + \frac{m_i \left(V_y^2 + V_x^2 \right)}{2} \right) \frac{n_i}{\tau_{cx}} + I_1 n \gamma_{ion} + \left(\frac{3}{2} \left(T_e + T_i \right) + \frac{m_i \left(V_y^2 + V_x^2 \right)}{2} \right) n \gamma_{rec} \tag{V.25}$$

or:

$$N_{ij}^1 = N_{ij} + dN_{i-1/2\,j}^x - dN_{i+1/2\,j}^x + dN_{ij-1/2}^y - dN_{ij+1/2}^y + \left(\gamma_{ion} - \gamma_{rec} \right) n V_{ij}^{cell} \tag{V.26}$$

$$P_{ij}^{x1} = P_{ij}^x + dP_{i-1/2\,j}^{xx} - dP_{i+1/2\,j}^{xx} + dP_{ij-1/2}^{xy} - dP_{ij+1/2}^{xy} - \gamma_{rec} V_{ij}^{cell} n V_{ij}^x \tag{V.27}$$

$$P_{ij}^{y1} = P_{ij}^y + dP_{i-1/2\,j}^{yx} - dP_{i+1/2\,j}^{yx} + dP_{ij-1/2}^{yy} - dP_{ij+1/2}^{yy} - \gamma_{rec} n V_{ij}^{cell} V_{ij}^y \tag{V.28}$$

$$E_{e;ij}^1 = \widetilde{E}_{e;ij} + dE_{e;i-1/2\,j}^x - dE_{e;i+1/2\,j}^x + dE_{e;ij-1/2}^y - dE_{e;ij+1/2}^y - \left(I_1 \gamma_{ion} + \frac{3}{2} T_e \gamma_{rec} \right) n V_{ij}^{cell} \tag{V.29}$$

$$E_{ij}^{i1} = \widetilde{E}_{ij}^i + dE_{i-1/2\,j}^{ix} - dE_{i+1/2\,j}^{ix} + dE_{ij-1/2}^{iy} - dE_{ij+1/2}^{iy} - \\ - \left(I_1 \gamma_i + \frac{3}{2} \left(T_e + T_i + \frac{m_i \left(V_y^2 + V_x^2 \right)}{2} \right) \gamma_r \right) n V_{ij}^{cell} \tag{V.30}$$

Define as: $P_{ij}^x = N_{ij} \widetilde{V}_{ij}^x$, $P_{ij}^y = N_{ij} \widetilde{V}_{ij}^y$, and (V.31)

$$dP_{ij+1/2}^{yy} = \left(n V^y \right)_{ij \pm 1} \widetilde{V}_{ij+1/2}^y S_{ij+1/2}^{cross}, \; dP_{ij+1/2}^{xy} = \left(n V^x \right)_{ij \pm 1} \widetilde{V}_{ij+1/2}^y S_{ij+1/2}^{cross} \tag{V.32}$$

$$dP_{i+1/2\,j}^{xx} = \left(n V^x \right)_{i \pm 1\,j} \widetilde{V}_{i+1/2\,j}^x S_{i+1/2\,j}^{along}, \; dP_{i+1/2\,j}^{yx} = \left(n V^y \right)_{i \pm 1\,j} \widetilde{V}_{i+1/2\,j}^x S_{i+1/2\,j}^{along} \tag{V.33}$$

$$dE_{ij+1/2}^y = e_{ij \pm 1} \widetilde{V}_{ij+1/2}^y S_{ij+1/2}^{cross}, \; dE_{ij+1/2}^x = \widetilde{e}_{i \pm 1\,j} \widetilde{V}_{i+1/2\,j}^x S_{i+1/2\,j}^{along} \tag{V.34}$$

$$dE_{e;ij+1/2}^y = e_{e;ij \pm 1} \widetilde{V}_{ij+1/2}^y S_{ij+1/2}^{cross} \;\; dE_{e;ij+1/2}^x = e_{e;i \pm 1\,j} \widetilde{V}_{i+1/2\,j}^y S_{i+1/2\,j}^{along} \tag{V.35}$$

Which are defined similar to $dN_{ij+1/2}^y$, see Eq. (V.18). Finally, in

the third sub-step we are calculating temperatures, velocity from momentum,

total energy and electron energy

$$n_{ij}^1 = \frac{N_{ij}^1}{V_{ij}^{cell}}, \quad \vec{V}_{ij}^1 = \frac{\vec{P}_{ij}^1}{N_{ij}^1}, \quad T_{e;ij}^1 = \frac{2}{3}\frac{E_{e;ij}^1}{N_{ij}^1}, \quad T_{i;ij}^1 = \frac{2}{3}\frac{E_{ij}^1 - E_{e;ij}^1 - \frac{m_i\left(\vec{V}_{ij}^1\right)^2}{2}}{N_{ij}^1}. \tag{V.36}$$

After these procedures the electron- and ion-thermo conductivities as well as the equipartition equations are solved as separate sub-steps of total time step.

$$\frac{\partial}{\partial t}\left(\frac{3}{2}n_e T_e\right) = n_e\frac{T_i - T_e}{\tau_E}, \qquad \frac{\partial}{\partial t}\left(\frac{3}{2}n_e T_i\right) = -n_e\frac{T_i - T_e}{\tau_E} \qquad \tau_E \equiv \frac{3m_i}{m_e}\tau_e \tag{V.37}$$

$$\frac{\partial}{\partial t}\left(\frac{3}{2}n_e T_e\right) + \frac{\partial}{\partial y}D_S^e T_e^{5/2}\frac{\partial T_e}{\partial y} + \frac{\partial}{\partial x}n_e D_\perp^e T_e\frac{\partial T_e}{\partial x} = -Q_{rad}\left(T_e, n\right) \tag{V.38}$$

$$\frac{\partial}{\partial t}\left(\frac{3}{2}n_e T_i\right) + \frac{\partial}{\partial y}D_S^i T_i^{5/2}\frac{\partial T_i}{\partial y} + \frac{\partial}{\partial x}n_e D_\perp^i T_i\frac{\partial T_i}{\partial x} = 0 \tag{V.39}$$

Here both thermoconductivity equations are solved implicitly, including the radiation term Q_{rad}:

$$\frac{3}{2}N_e\frac{\partial T_e}{\partial t} = \kappa\left(T_e\right)\frac{\partial T_e}{\partial y}\Bigg|_-^+ + \dot{Q}_{rad}(T)V_{cell} \tag{V.40}$$

$$\frac{3}{2}N_{eij}\frac{T_{ij} - \widetilde{T}_{ij}}{\Delta t} = \kappa_{ij+1/2}\frac{T_{ij+1} - T_{ij}}{\Delta y} - \kappa_{ij-1/2}\frac{T_{ij} - T_{ij-1}}{\Delta y} + \dot{Q}_{rad}\left(\widetilde{T}_{ij}\right) + \frac{\partial\dot{Q}_{rad}\left(\widetilde{T}_{ij}\right)}{\partial T}\left(T_{ij} - \widetilde{T}_{ij}\right)V_{cell} \tag{V.41}$$

$$\begin{aligned}\frac{\kappa_{ij+1/2}\Delta t}{\Delta y}T_{ij+1} - \left(\frac{3}{2}N_{eij} + \frac{\partial\dot{Q}_{rad}\left(\widetilde{T}_{ij}\right)}{\partial T}\Delta t V_{cell} + \frac{\kappa_{ij-1/2}\Delta t}{\Delta y} + \frac{\kappa_{ij+1/2}\Delta t}{\Delta y}\right)T_{ij} - \frac{\kappa_{ij-1/2}\Delta t}{\Delta y}T_{ij+1} = \\ \left(\frac{3}{2}N_{eij} + \frac{\partial\dot{Q}_{rad}\left(\widetilde{T}_{ij}\right)}{\partial T}\Delta t V_{cell}\right)\widetilde{T}_{ij} - \dot{Q}_{rad}\left(\widetilde{T}_{ij}\right)\Delta t V_{cell}\end{aligned} \tag{V.41}$$

VI. Physic Models of plasma transport in the SOL/Divertor. Scaling laws and simple models for benchmarking

In this part we present three different regimes of the SOL and divertor operation, which is observed in tokamaks, depending on the level of plasma recycling on the divertor plates. These are of low, intermediate and high recycling regimes of operation, corresponding to attached, partly detached and fully detached cases correspondingly. The regimes are characterized by specific plasma behavior and their features can be described by a physics models, allowing simple solutions, which can be compared with the full scale 2D simulations in TOKES and used for benchmarking.

One of the main tasks of plasma modeling in the SOL and divertor region is to establish scaling laws at the separatrix between bulk and edge plasma parameters. This means e.g., the connection between the temperature T_s and the density n_s at the separatrix with the particle and energy fluxes, coming from the bulk plasma through the separatix, Q_s and Γ_s. The boundary conditions can also be expressed through the plasma parameters at the divertor plate, using a link between density, temperature and fluxes at the separatrix and at the plate.

First, we consider the simplest models, for two limiting cases of low and high recycling near the material surfaces. The schematic of the SOL and divertor configuration is shown on the Fig.12.

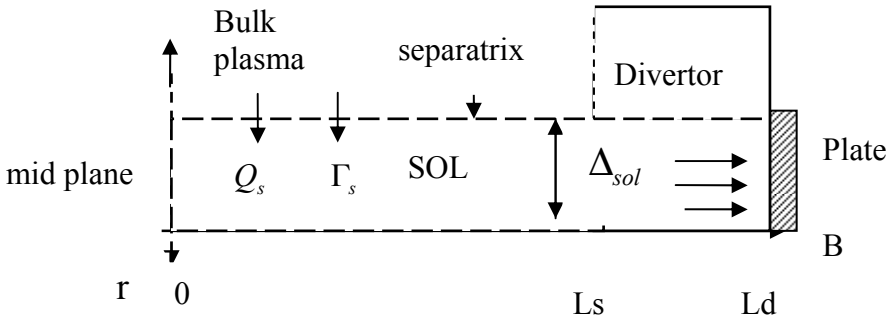

Fig.12 Model of boundary plasma

The plasma heat Q_s and particle flux Γ_s flow through the separatrix into the SOL region L_s with and divertor region L_d (see Fig. 12). For self-consistent calculations of the balk and the boundary plasma it appears convenient to use boundary condition at the separatrix in the form $T_s(Q_s,\Gamma_s)$ and $n_s(Q_s,\Gamma_s)$.

VI. 1. The case of low recycling

The contribution of neutral atoms into plasma flux due to ionization is described by recycling coefficient, R , defined as:

$$R = \left(\Gamma_d - \Gamma_s\right)/\Gamma_d \qquad \text{(VI.1)}$$

In the case of low recycling, considered below, $R \sim 0$, the plasma parameters remain almost constant along the magnetic field lines, the convective energy loss to the divertor plates dominates the parallel transport with the sound speed velocity,

$$C_s = \left(T_s / m_i\right)^{1/2} = C_{s0} \cdot T_i^{1/2},\ m/s \qquad C_{s0} \equiv 9.79 \cdot 10^3 / \sqrt{\mu} \qquad \mu \equiv m_i / m_p \qquad \text{(V1.2)}$$

at the plate, where m_i is the mass of the dominant ion component, m_p is the proton mass and the radial (perpendicular) transport is described usually as a diffusion with some anomalous coefficient, $D_\perp$. Historically, it is taken as a Bohm value, either constant or as a function of parameters at the separatrix:

$$D_B = cT_s / 16eB = D_0 \cdot T_s / B_T,\ m^2/s,\ D_0 \equiv 6.25 \cdot 10^{-2} \qquad \text{(VI.3)}$$

where B_T is the magnetic field in Tesla. The diffusion normal to the magnetic surfaces, ψ, in the rear SOL plasma reads as:

$$D_B \frac{\partial^2 n}{\partial r^2} - \frac{n}{\tau_{//}} = 0 \qquad \text{(VI.4)}$$

where $\tau_{//} = L/C_s$, $L \approx \pi q R$ is the magnetic field line length, q is the safety factor at $\psi = 95\%$, R is the major radius and n is the density averaged over the magnetic surface ψ, and $r = \sqrt{\psi}$ marks the magnetic surfaces. Equation (VI.4) is averaged along the field lines and the parallel flow, described as a loss term (last term in (VI.4)). This is justified because the plasma parameters are almost homogeneous along the field lines and D_B is taken const.. The density decay length in the SOL is of the order of gyro-radius only in the case of classical diffusion across, $\Delta_n = \sqrt{D_{cl} \cdot \tau_{//}} \propto \rho_c$ and usually always exceeds ρ_c in the case of anomalous diffusion, for example: $\Delta_n = \sqrt{D_B \cdot \tau_{//}} \approx \rho_c (\omega_c \tau)^{1/2} \left(\frac{L}{\lambda_{ei}}\right) >> \rho_c$ in the Bohm case. Here, ω_c is the gyro frequency and τ is the electron-ion coulomb collision frequency, $\lambda_{ei} \equiv V_T \tau$ is the mean free pass, V_T is the thermal velocity. In the case of rear plasma, $L \le \lambda_{ei}$. Since the temperature decay length in the SOL is typically $\Delta_T \approx \Delta_n / 3$, the fluid treatment of plasma behavior in the SOL region is applicable. For high-energetic particles, emerging from the core region the gyro-radius can exceed the SOL width. In the case of ITER for expecting temperatures at the separatrix (~300eV) , $\Delta_{sol} / \rho_c \approx 50$ and for pedestal temperatures

(~3keV), $\Delta_{sol} / \rho_c \approx 20$. Only for the high-energetic alpha-particles with energies ~0.5 MeV the gyro radius (or the banana width) becomes comparable with the SOL thickness. These particles are considered as prompt lost particles, or the particles escaping the main plasma due to the loss-cone inside the LCFS. Equation (VI.4) gives an exponential decay of density across the SOL:

$$n(r) = n_s \cdot \exp\left(-(r-a)/\Delta_n\right) \qquad \text{(VI.6)}$$

where R and a are the major and the miner radius of tokamak plasma, respectively and

$$\Delta_n = 3.18 \cdot 10^{-3} \sqrt{L[m]/B[T]} \cdot T_{s,eV}^{1/4},\ m\,. \qquad \text{(VI.7)}$$

The particle and energy fluxes along the magnetic field line remain constant throughout the SOL and can be written as particle flux, Γ_d, and thermal power, Q_d to the plate:

$$\Gamma_s \approx \Gamma_d = 0.25 M n_s C_{s0} \sqrt{T_s} \cdot S_{\perp sol} \quad \text{and} \quad Q_d \approx Q_s = 5 \cdot \Gamma_s T_s \qquad T_s \equiv T_{s,e} \sim T_{s,i} \qquad \text{(VI.8)}$$

where Q_s is the total power into the SOL region and the SOL cross-section surface $S_{\perp sol} = \pi(a+\Delta_s)^2 - \pi a^2 \approx 2\pi a \Delta_s$. Here Δ_s is the SOL width and M is the Mach number near the divertor plate, which is close to one. If $\Delta_s \approx \Delta_n$, then

$$\Gamma_s \approx (\pi a M C_{s0} S_{\perp sol}/2) n_s \sqrt{T_s} \cdot \sqrt{D_B \tau_{//}} \approx 30.9 \cdot S_{\perp sol} \left(aM \cdot L/\sqrt{B}\right) \cdot n_s T_s^{3/4},\ 1/\text{sec} \qquad \text{(VI.9)}$$

$$Q_s = 5 k_b \cdot \Gamma_s T_s,\ MW \qquad \text{(VI.10)}$$

From (VI.9, VI.10) follow the relations, which can serve as boundary conditions at the separatrix:

$$n_s[m^{-3}] = Const. \left(\Gamma_{s,}[s^{-1}]\right)^{7/4} \cdot \left(Q_s[MW]\right)^{-3/4} \qquad \text{(VI.11)}$$

$$T_s,[eV] = Q_s[MW] / 5 k_b \Gamma_s[s^{-1}] \qquad \text{(VI.12)}$$

where $Const. = 4.3 \cdot 10^{18} \cdot \sqrt{B_T} / \left(S_{\perp sol}[m^2] \cdot a[m] M \cdot L[m]\right)$

The specific feature of the simplified model is the monotonic dependence of density and temperature on fluxes, which excludes the occurrence of bifurcation in the boundary region. At high plasma temperatures due to strong dependence of parallel heat conductivity on temperature and the long connection length the slight variation of the temperature and density along the magnetic field lines can occur. In this case the density and temperature at the plate n_p, T_p must be estimated from the conductivity and pressure balance equations along the magnetic field lines, *s*:

$$\frac{\partial q}{\partial s} = Q_s / V_{SOL} - Q_{rad}\,; \qquad q = -\chi_0 T^{5/2} \frac{\partial T}{\partial s} \qquad \text{(VI.13)}$$

$$n_{mid}T_{mid} = (1+\gamma M^2)n_d T_d \qquad \text{(VI.14)}$$

Here $V_{SOL} = 2\pi^2 R\Delta_{sol} a(1+K) \approx S_{\perp SOL} \cdot 2\pi R$, where $K = b/a$ is the elongation and Q_{rad} are the radiative losses in the SOL/divertor region, $\gamma = 5/3$. Equations (VI.13, VI.14) are averaged over the SOL width. The density and temperature at *s = 0* represent the upstream or the mid-plane values and the Spitzer-Harm parallel conductivity, $\chi_0 = 1.3\cdot 10^{22} m^{-1}s^{-1}eV^{-5/2}$ is assumed. Integrating the equations (VI.13) first in the SOL region L_s, with the source term Q_s and then, in the divertor region $L_d = L - L_s$, where $Q_s = 0$, one finds:

$$T_d^{7/2} = T_{mid}^{7/2} - T_*^{7/2}, \qquad \text{(VI.15)}$$

where

$$T_*^{7/2} \equiv \left(\frac{7L_s^2 Q_s}{4\chi_0 V_s}\right)\left((1-f_{rad})\cdot(1+2L_d/L_S)\right) \qquad f_{rad} \equiv \frac{Q_{rad}}{Q_s/V_s} \qquad \text{(VI.14)}$$

and

$$n_d \approx n_{mid}T_{mid}/2T_d \quad (M=1), \qquad \text{(VI.15)}$$

Here T_* denotes the minimum temperature, which can be achieved at the mid-plane for given Q_s and for given level of radiation losses, f_{rad}. The dependence $T_{up}(T_d)$ which follows from classical electron thermal conductivity is shown in the Fig. 13. If $T_{mid} >> T_*$, then $T_p \approx T_{mid}$, when $T_d \le T_*$, T_{mid} reaches its minimum value T_* . This occurs due to strong dependence of classical conductivity on temperature.

$$T_*, eV \equiv 7.0\left(\left(L_S[m]\right)^2 \cdot Q_s[MW]\cdot\left(\left(1-f_{rad}\right)\cdot\left(1+2L_d/L_S\right)/V_s[m^3]\right)\right)^{2/7} \qquad \text{(VI.16)}$$

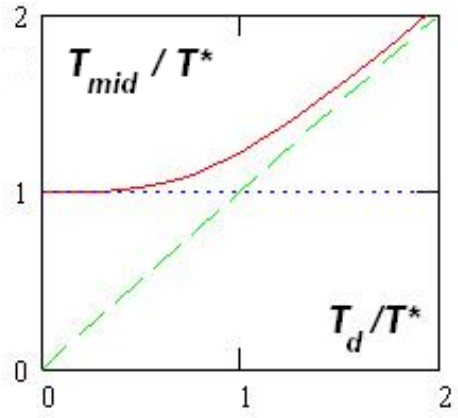

Fig.13 The dependence $T_{up}(T_d)$ which follows from classical electron thermal conductivity; if $T_{mid} >> T_*$, then $T_d \approx T_{mid}$, when $T_d \le T_*$, T_{mid} reaches its minimum value T^* . This occurs due to strong dependence of classical conductivity on temperature.

In the ITER case, for $L \sim 190m$ and $Q_s L_s / V_s \sim 1380\, MW/m^2$, the critical seperatrix temperature (VI.14) is $T_* \sim 0.3\, keV$. This is the minimum achievable upstream temperature for given power and connection length values. If downstream temperature drops below the critical one a noticeable gradient develops, which keeps the mid-plane temperature almost unchanged. This occurs due to strong dependence of classical conductivity on temperature. The radiation losses bring down the upstream temperature.

VI. 2. The case of intermediate / high recycling (attached plasma)

In this case $R \le 1$ in the vicinity of the plate and the associated radiation brings down the temperatute there. Recycling considerably amalgamates the particle flux to the plate. Although the density and the temperature strongly vary, the pressure along the magnetic field lines remains roughly constant. Under this condition, when the temperature at the plate is small the thermal conductivity becomes a dominant transport mechanism along the magnetic field lines $\chi_{//} = \chi_0 \cdot T^{5/2}$. For given n_s at the separatrix and given parameters Q_s, R, f_{rad} the functions $T_s(Q_s, n_s)$, and $\Delta_T(Q_s, n_s)$ can be easily derived from the energy balance equation (VI.13). Using for the anomalous radial conductivity the following scaling: $\chi_\perp = \chi_\perp^0 \cdot T_s^c \cdot n_s^b$, one finds:

$$T_s = \left(\frac{\left(Q_s^2 (1 - f_{rad}\right)^2 L^2 / S_\perp^2}{\chi_{//}^0 \chi_\perp^0 n_s^b} \right)^{2/(2c+9)} \qquad \text{(VI.2.1)}$$

$$\Delta_T = \frac{R}{\chi_{//}^0} \left(\frac{\chi_{//}^0 \chi_\perp^0 n_s^b}{\left(Q_s \cdot (1 - f_{rad})\right)_s^{(5-2c)/7}} \right)^{7/(2c+9)} \qquad \text{(VI.2.2)}$$

Here $\Delta_T \equiv \partial x / \partial \ln T$ is the thermal layer width ($\Delta_T \propto \Delta_n / \sqrt{3} < \Delta_{sol}$), $\chi_\perp^0 \approx D_0 / B_T$ and the exponents here are arbitrary numbers. The dependence of temperature and density at the divertor plate on separatrix density can be derived again from the condition of constant pressure along the magnetic field line (note, that the separatrix and the mid-plane values, indicating with the subscript *s* and *mid*, and the values denote as *p* and *d* at the plate are roughly the same):

$$n_s T_s = (1 + \gamma M^2) n_p T_p \approx 2 n_p T_p, \qquad \text{(VI.2.3)}$$

and the particle balance in the recycling zone in the vicinity to the plate:

$$\left(1 + \gamma M^2\right) C_{s0} n_p T_p^{3/2} \approx \frac{\Gamma_s}{(1 - R)}, \qquad \text{(VI.2.4)}$$

where R is the recycling coefficient, which is taken here as a given value. The particle flux at the plate now reads as:

$$T_p = \frac{1}{n_p}\left(\frac{Q_s^2(1-f_{rad})^2}{\chi_{//}^0\chi_{\perp}^0}\right)^{2/(2c+9)} n_s^{\frac{2(c-b)+9}{2c+9}} \qquad \text{(VI.2.5)}$$

and n_p can be found from (VI.2.4). One can notice a rather weak dependence of edge plasma parameters (n_s, Δ) on separatrix density n_s and the heat flux Q_s due to strong dependence of parallel thermal conductivity on plasma temperature. In reality the recycling coefficient R depends on plasma parameters. The total plasma flux to the plate $\Gamma_p = \Gamma_s + R \cdot \Gamma_p$ consists from the initial flux Γ_s and from the contribution $R \cdot \Gamma_p = \Gamma_{ion}$, arising due to ionization of neutrals:

$$\Gamma_{ion} = \eta \cdot \Gamma_p \cdot (1 - \exp-(\int dx / \lambda_{ion})) \qquad \text{(VI.2.7)}$$

were η is the recombination coefficient at the plate surface, $\lambda_{ion} = V_0(T_p)/n_p\langle\sigma V\rangle_{ion}$ is the ionization mean free pass of neutrals.

Dependence of plasma parameters at the plate from separatrix density can also be derived from energy and pressure balance:

$$T_p = \frac{1}{n_s^3}\left(q_{\perp}^{10}\frac{\chi_{//0}^6}{\chi_{\perp 0}^3 L}\right)^{2/11} \qquad \text{(VI.2.8)}$$

$$n_p = \frac{n_s^{3/7} q_{\perp}^{-16/11}}{(1-R)}\left(\frac{\chi_{\perp 0}^4 L^3}{\chi_{//0}^7}\right)^{2/11} \qquad \text{(VI.2.9)}$$

where $q_{\perp} = Q_{s,\perp}(1-f_{rad})/S_{\perp}$.

These equations show how scales density and temperature in mid-plane and divertor plate with machine size (*R, a*) and the heat flux in the SOL, $S_{\perp} \approx 2\pi^2 Ra \cdot \left(1.5 \cdot (1+K) - \sqrt{K}\right)$, where *K* is the elongation. The scaling law correspond to high recycling regimes in the SOL with classical heat conduction along the magnetic field lines and Bohm conduction (*b=1, c=1*) across field lines. Note, however, that in the model parameters R and f_{rad} are independent. One can see from (VI.2.8, VI.2.9) that the plasma temperature at the plate, decreases as the inverse cube of the thermal layer density and depends weakly on the field line length, *L*. In addition, any variation in the input heat flux and in the parallel heat conduction can strongly affect temperature at the plate. The thermal width scaling is important, since it determines the peak power load on the plate. Although we are operating here with the density profile width

value, it is worth to note, that the radial density profile in the SOL is not described any more by simple exponential form (VI.1.4), because the source of neutrals due to ionization plays an important role in density profile formation.

IV. 3. The case of high recycling (detached plasma)

This is the case, when plasma detaches from the plate and almost all power in the SOL/divertor region is radiated by impurities and by hydrogen. A significant pressure drop along the magnetic field lines occurs and the plasma density drops towards the plates. The main signatures of detachment include also the plasma particle drop at the plate (ion saturation current) and the formation of a strong radiating zone (radiative blanket in divertor), which cools down the plasma and radiates almost 100% of energy. The SOL and divertor area can be divided into two zones, the upstream radiative zone and the neutral gas dominating downstream area with the rear cold plasma, so called cushion near the plate. A schematic of the divertor plasma between the X-point and the target is shown in Fig. 14.

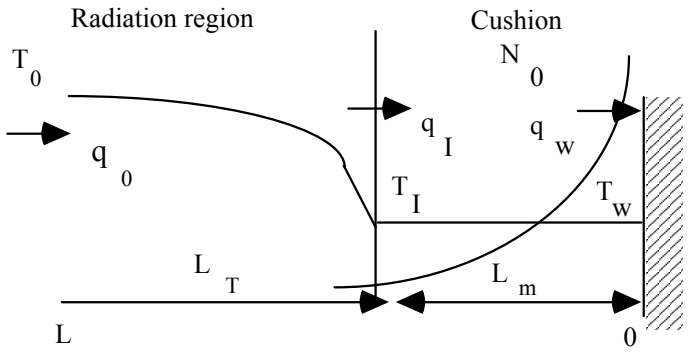

Fig. 14 Schematics of divertor plasma in detached state

Two regions are indicated: the radiation region and the cushion (gas blanket). In the radiation region, energy losses occur due to the radiation of impurity ions (e.g. Be etc.) and the power is transported by parallel heat conduction. In the right-hand part of the cushion, the plasma is cold and the remaining power is so small that ionisation is excluded and temperature is taken to be constant along the region ($T_I=T_W$). Convection dominates the heat flow in this region. In the vicinity of the interface between the two regions, ionisation takes place. In this model we are not specifying the position of the border between these two regions, assuming that the cushion will be self-consistently developing according to the balance equations. In the cushion, a charge exchange collisions with neutrals cause the parallel momentum loss from

the plasma flow, thus reducing the pressure at the plate. Detachment occurs when the radiation is strong enough to limit the ionization capability downstream of the radiating region. In order to simulate this complex phenomenon a simplest model is chosen below, which, however, preserves the main features of detachment. This model provides necessary for benchmarking solutions of reduced equations.

The 1D equations for energy, particle and momentum balance along the field lines in the SOL are employed [33]:

$$\frac{\partial q}{\partial x} = n n_z L(T) \qquad \text{(VI.3.1)}$$

$$\frac{\partial \Gamma}{\partial x} = \frac{n_{//}}{\tau_\perp} \qquad \text{(VI.3.2)}$$

$$\frac{\partial (p + mnV^2)}{\partial x} = -\frac{nmV}{\tau_\perp} \qquad \text{(VI.3.3)}$$

where q and Γ are the heat and the particle fluxes along the magnetic field lines, n and n_z denote the plasma and impurity density, $L(T)$ is the radiation cooling rate , V is the parallel velocity, $\tau_\perp$ is the particle (momentum) loss time due to a radial diffusion $\tau_\perp \sim \Delta^2 / D_\perp$ and a charge-exchange collision τ_{cx}, $\tau_\perp^{-1} = \tau_{dif}^{-1} + \tau_{cx}^{-1}$. For given density n_s , temperature T_s and heat flux q_s at the separatrix, the plasma parameters at the plate and conditions for detachment can be uniquely defined from equations (VI.3.1- VI.3.2). A transition from attached to detached state at given upstream conditions can be triggered by varying the impurity content in divertor, thus increasing the radiation losses in divertor region.

The seven unknown parameters, which must be defined are , the heat and particle fluxes q_{pl}, Γ_{pl} at the plate, the temperature T_{pl} at the plate , the neutral density n_0, fraction of radiation, f_{rad}, fraction of momentum loss due to interaction with neutrals, f_m, and the length of the cushion, L_m. Upstream heat flux, q_{up} and upstream pressure, p_{up} together with impurity concentration are the free parameters. The seven required equations are the following:

1) $$n_s = (1 - f_m) p_s / \left(1 + \gamma M^2\right) T_{pl} \qquad \text{(VI.3.3)}$$

where f_m is the momentum loss fraction defined as $f_m \equiv (p_s - p_{pl}) / p_{pl}$ and T_{pl} is the temperature at the plate and M is the Mach number at the plate, which is according the Bohm requirements is about 1.

The equation for energy remaining in plasma after radiation is transferred to the plate

2) $q_{pl} = \Gamma_{pl}\left(\varepsilon + \delta T_{pl}\right)$ (VI.3.4)

where $\varepsilon = 20$, $\delta = 7.8$ .Multiplying Eq.(VI.3.1) by $q = -\chi_0 T^{5/2}\partial T/\partial x$ and then, integrating from upstream to downstream, one has

Energy balance equation upstream of the cushion

3) $q^2(T) = q_I^2 + \dfrac{\chi_0 p_{up}^2 c_Z}{2}\int_{T_I}^{T}\sqrt{T}L(T)dT$ (VI.3.5)

where q_I and T_I are the heat flux and plasma temperature at the end of the radiation zone, and $L(T)$ is the radiation loss function. C_Z is the impurity concentration, p_{up} is the upstream pressure.

Equation for the length of the radiation zone, L_r, which can be determined from the local heat flux by

4) $L_r = \chi_0 \int_{T_I}^{T_{up}} \dfrac{T^{5/2}}{q(T)}\,dT = L - L_m$ (VI.3.6)

and is equal to the difference between L (total connection length between X-point and plate) and the cushion length. T_{up} is the upstream temperature $\left(T_{up} \approx T_s\right)$. We also assume constant temperature in the cushion. Notice, that relation between the upstream heat flux q_{up} along the magnetic field lines and q_s - across the LMFS. Since at separatrix $divq$ ~0, then

$q_{up} = q_s \dfrac{2\pi q_\psi a}{\Delta_{sol}}$, where q_ψ is the safety factor.

The equation for radiation fraction, which follows from the energy balance in the cushion

5) $f_{rad} \cong 1 - \dfrac{p_{up}}{q_{up}}(1 - f_{mom})\dfrac{M}{1+M^2}\dfrac{(\varepsilon + \gamma_t T_d)}{\sqrt{T_d}}$ (VI.3.6)

This relation shows that at given p_{up} and q_{up} the achievement of detachment ($f_{rad} \sim 1$) is limited by momentum loss efficiency, f_{mom}!

6) Equation for momentum loss fraction is derived in (see [33])

$$f_m = 1 - \exp(-L_m / \lambda^*); \qquad \text{(VI.3.7)}$$

where $\lambda^* = 2.398 \cdot d(m)(11.51 \cdot Kn + 1)$ is an effective length (in *m*) for the momentum loss, L_m is the cushion length, *d(m)* is the plasma-wall distance and *Kn* is the Knudsen number for neutrals *Kn* = 2.5 10^{19} m^{-3} / ($d(m) \cdot n_0(m^{-3})$).

Equation for neutral density:

$$7)\ \Gamma_{//} \exp(-\Delta / \lambda_{ion}) A_1 = \frac{B_{//}}{B_p} n_0 (C_{pump} + \frac{A_0}{4} v_0 (1 - \eta)\ ), \quad A_1 = 2\pi R\Delta \qquad \text{(VI.3.7)}$$

This is the particle balance equation in the divertor. The neutral density n_0 in the divertor region is found from a simplified model (shown schematically in Fig. 15).

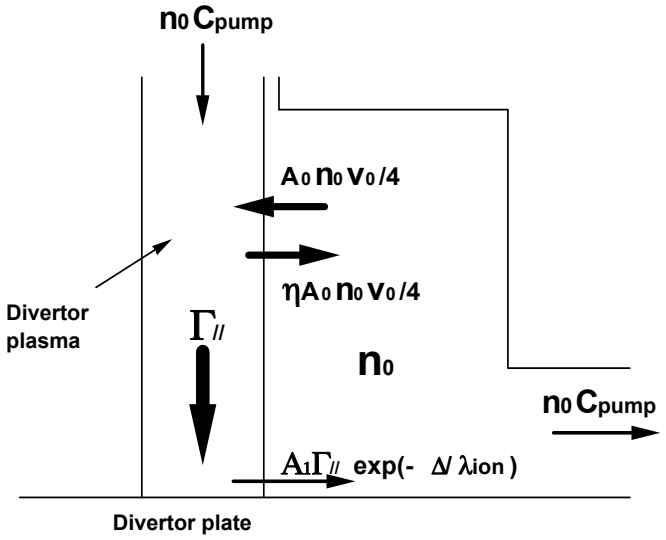

Fig. 15 Model of divertor chamber and pumping port.

A fraction of the recycling ion flux determined by the ionisation mean free path λ_{ion} escapes from the plasma column (width Δ) and forms the source of the neutrals. There are two sinks of neutrals. One part is pumped (n_0 C_{pump}; this also equals the net incoming ion flux from upstream). Another part, $An_0v_0/4$, enters the plasma column with thermal speed v_0 and a fraction η of these neutrals is again reflected back to the vacuum region due to charge exchange collisions. In equation $B_{//}$ and B_p are parallel and poloidal magnetic field,

respectively, A_0 is a typical area for the plasma column. For simplicity, we take here $A_0=A_1$ (A_1 is the cross-sectional area), but this could be generalized.

The seven equations listed above contain seven unknown variables Γ, q_I, T_I, T_{up}, n_0, L_m and f_m. They can be solved as function of C_Z for given upstream power and pressure.

Calculations were performed for typical ITER conditions: input heat flux $q_{//}$=650 MW/m^2, upstream pressure (ion + electron) p=3200 Pa, connection length L= 40 m, angle of incidence between the field line and the target plate α=7.2°, and various Cz for Be ion concentrations. The main results are the following:

The detachment is caused by increased radiation because the power available for ionization is reduced. Recycling, neutral density, and momentum loss adjust self-consistently during the transition. The transition is gradual with increasing impurity concentration, i.e. no bifurcation exists. It should be noted that the transition from attached to detached corresponds to a small change in impurity concentration.

The increase of neutral density and decrease in particle flux which have been shown to accompany the transition are consistent with experimental observations. This increase of neutral density leads to higher momentum loss, f_m. Beyond the transition, the ionization mean free path becomes so long that the neutral loss from the plasma becomes independent of the mean free path and then the neutral density varies simply with the particle flux, i.e. decreases somewhat with increasing C_Z . This decrease is not important: the plasma remains detached. In the final detached state at high C_Z, the heat flux and particle flux are low and the cushion length and momentum loss are high.

IV. 4. The benchmarking of TOKES result with simple transport models in the SOL.

Here we are comparing the solutions of reduced equations (Belocerkovsky in y-direction)

$$\frac{\partial n}{\partial t} = -\frac{\partial}{\partial y}\left(nV_y\right) + \frac{\Gamma}{V_{SOL}} \qquad \text{(IV.4.1)}$$

$$\frac{\partial nV^y}{\partial t} + \frac{\partial}{\partial y}\left(nV^yV^y\right) = -\frac{\partial 2nT}{m\partial y} \qquad \text{(IV.4.2)}$$

$$\frac{\partial}{\partial t}\left(3nT\right) + \frac{\partial}{\partial y}\left(5nT\right)V_y = \frac{QQ}{V_{SOL}} \qquad \text{(IV.4.3)}$$

with exact analytic solution of this system (or derived by MathCAD) with TOKES solution for several input parameters (particle and heat flux).

I=2*10^{22} s^{-1} and QQ=20 MW:

TOKES SOLUTION	ANALYTICAL SOLUTION
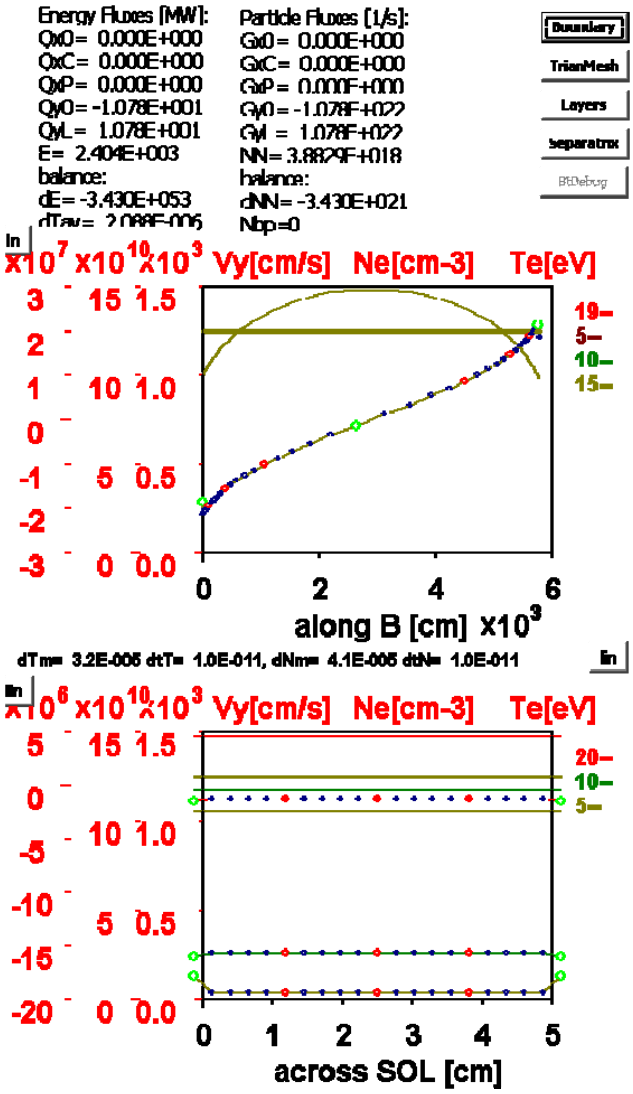	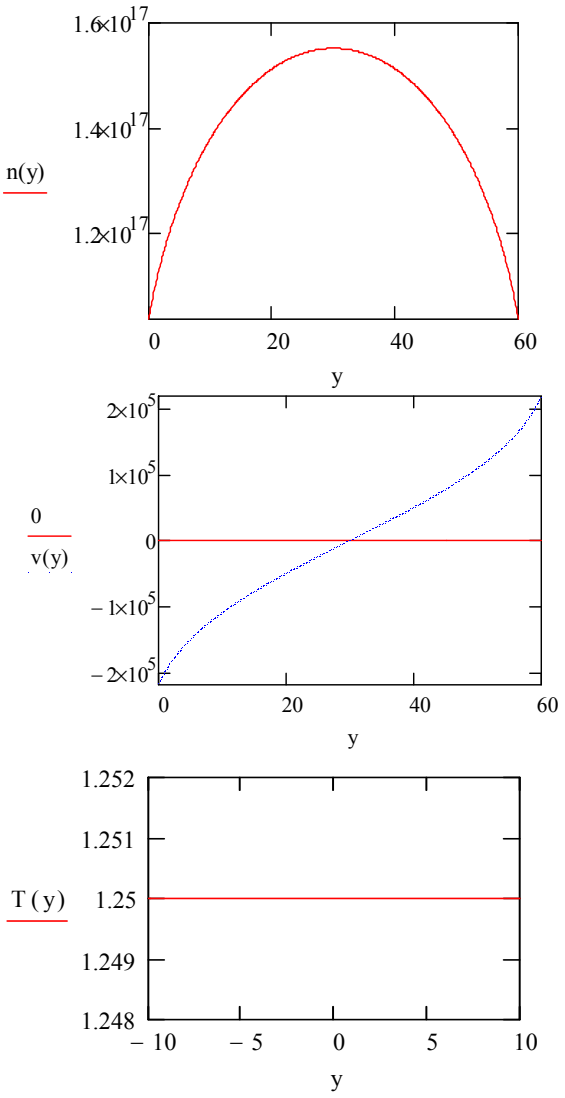

Here $v(0) = -2.189 \times 10^5$ $v\left(\frac{L}{2}\right) = 0$

$v(L) = 2.189 \times 10^5$

$nw = 1.034 \times 10^{17}$

$n\left(\frac{L}{2}\right) = 1.551 \times 10^{17}$

The same comparison with other input parameters and distributed power along B:

I=2*10^{22} s^{-1} and $QQ = 20\left(1 - \left|\frac{2y}{L} - 1\right|\right) MW$. In this case the analytical solution reads:

$$n(y) := \frac{3}{4}\cdot\frac{n0}{\left(1+2\cdot\frac{y}{L}\right)} + \sqrt{\left[\frac{3}{4}\cdot\frac{n0}{\left(1+2\cdot\frac{y}{L}\right)}\right]^2 - Sn^2\cdot\frac{\left(y-\frac{L}{2}\right)^2}{Cs(Tmax)^2\cdot\left(1+2\cdot\frac{y}{L}\right)}}$$

$$V(y) := \frac{Sn}{n(y)}\cdot\left(y-\frac{L}{2}\right) \qquad T(y) := \frac{Tmax}{2}\cdot\left(1+2\cdot\frac{y}{L}\right) \qquad Tmax := Sq\cdot\frac{k}{5\cdot Sn}$$

$$n\left(\frac{L}{2}\right) = 1.097\times10^{17} \qquad n(0) = 1.463\times10^{17} \qquad V(0) = -1.548\times10^{5}$$

,

TOKES SOLUTION	ANALYTICAL SOLUTION
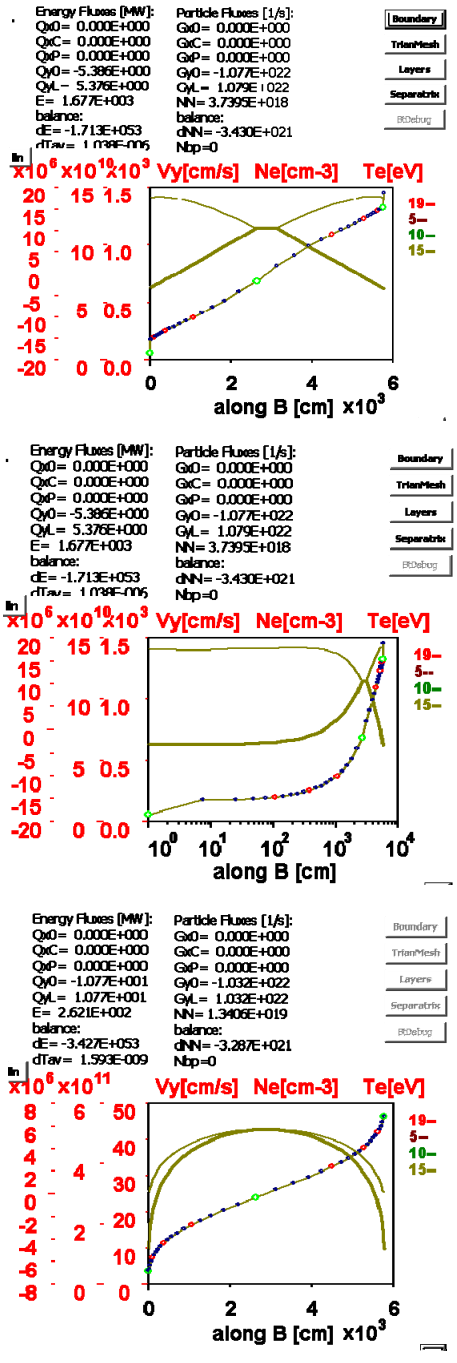	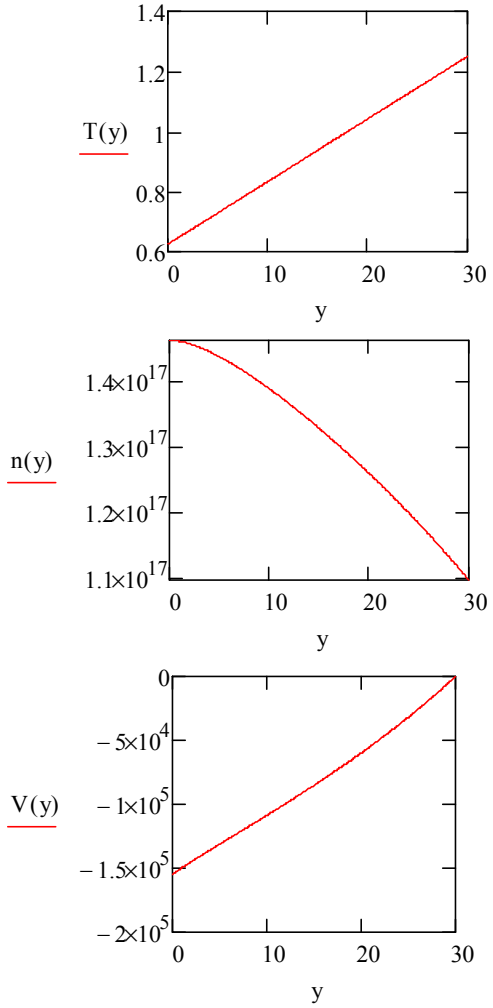

VII. Model for H-Mode Pedestal formation in TOKES

During the L to H-mode transition, when input power, Q .exceeds some critical value, Q_{LH} [5]:

$$Q_{LH} = 0.084 \cdot \bar{n}^{0.73} B_T{}^{0.74} S^{0.98} M^{-1} \qquad \text{(VII.1)}$$

a strong pressure gradient forms at the edge because of the turbulent transport suppression outwards beyond some radial position. This pressure gradient separates the anomalous core and the neoclassical pedestal region, which spreads from the top of the pedestal up to separatrix and is is marginally stable. There are two suppression factors: 1) proportional to $1/\left(1 + k \cdot (\omega_{ExB}/\gamma)^2\right)$, where γ is an increment of the ion temperature gradient (ITG) instability and ω_{ExB} is *ExB* shearing rate, and 2) due to increase of edge (e.g. bootstrap) current and, consequently, the magnetic shear at the edge. Since $\gamma \sim 1/s$, increase of shear suppresses the turbulence. We assume here, that the turbulent transport is mainly suppressed by $\boldsymbol{E_r \times B}$ velocity shear at the plasma edge. This means, that the radial transport coefficients for thermal conductivity and particle diffusion drop down to subdominant (neoclassical) value:

$$\chi_{e,i} = \chi_{e,i}^{an} \cdot \left\{ 1 + k \cdot \left(\frac{\omega_{ExB}}{\gamma(s)} \right)^2 \right\}^{-1} + \chi_{e,i}^{neo} \qquad \text{(VII.2)}$$

$$D_{e,i} = \chi_{e.i} \cdot n \qquad \text{(VII.3)}$$

Here $\chi_{e,i}^{an}$ is the anomalous conductivity, which dominates in the core region, where $\gamma > \omega_{ExB} \sim 0$. Within pedestal region, where $\gamma < \omega_{ExB}$, anomalous transport is suppressed by the magnetic shear *s* and *ExB* shear. In this region the dominate transport is neoclassical (second term in (4)). Here *k* is some fitting factor~1. The anomalous conductivity is

$$\chi_{e,i}^{an} = \chi_{GB} \approx \rho_{tor}^2 C_s / s^{\varepsilon} \Delta_{ped} \qquad \text{(VII.4)}$$

and

$$\gamma_s = \chi_{GB} k_\perp^2 \approx \rho_{tor}^2 C_s k_\perp^2 / s^{\varepsilon} \Delta_{ped} \qquad k_\perp^2 \rho_{tor}^2 \approx 0.03 \qquad \text{(VII.5)}$$

where γ is the growth rate of a gyro-Bohm type instability. Expression for shearing rate ω_{ExB} reads as:

$$\omega_{ExB} = \frac{\partial}{\partial r}\left(\frac{E_r}{B}\right) \approx \frac{\partial}{\partial r}\left(\frac{\nabla p}{n \cdot B}\right) \approx \rho_{tor} C_s / \Delta^2_{ped} \qquad \text{(VII.6)}$$

Here we assume, that $E_r \approx en\nabla p$ and $\nabla p \approx nT / \Delta_{ped}$ .The width of the pedestal region, Δ_{ped} , can be defined as a radial position inside the separatrix , where turbulence is suppressed by the combined effect of the magnetic and $\boldsymbol{E} \times \boldsymbol{B}$ shear (see Figs. 17). The pedestal width depends on the toroidal Larmor radius ρ_{tor} and the magnetic shear $s(r)$, and can be expressed as:

$$\Delta_{ped} = \rho_{tor} \cdot s^2 \qquad \rho_{tor} = 3.23 \cdot 10^{-3} \cdot B_T^{-1} Z^{-1} \sqrt{A \cdot T_{i,}} \qquad \text{(VII.7)}$$

Here B_T is the toroidal magnetic field in Tesla, A is the mass number, Z is the charge state, T_i is the ion temperature in keV, ρ is in m. The shear depends on radial position, but for simplicity sake it can be arbitrarily chosen at 95% flux surface.

The pedestal width, Δ_{ped} be define as a radial position where :

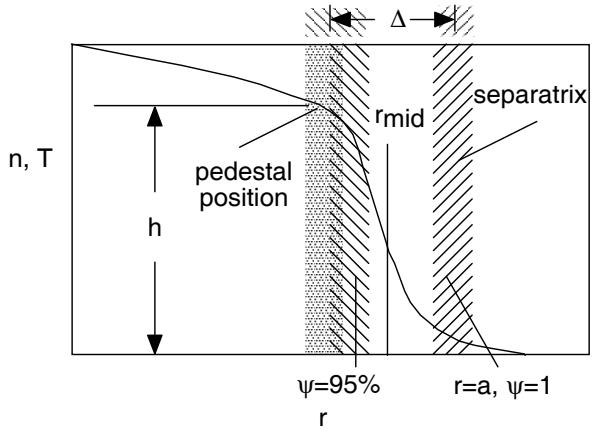

Fig. 16 *Definition of pedestal width.*

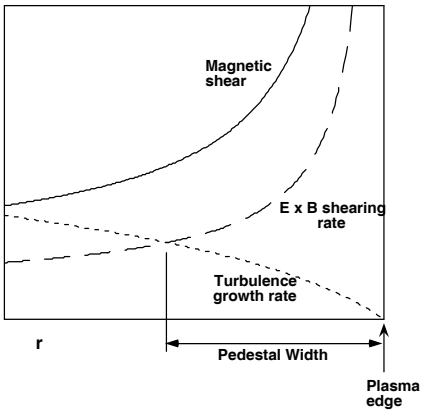

Fig. 17 *Pedestal width is define at radial position where turbulence is suppressed by magnetic and electric shear.*

The radial transport suppression in TOKES , which describes the L to H transition is implemented (taking into account threshold dependence of the H-mode onset on input power) as

$$\chi = \frac{\chi_{an}}{1 + \mu\theta(Q - Q_{LH})(s^2 \rho_i / k_{ped})^2} + \chi_{neo} \qquad \text{(VII.8)}$$

where $\Delta_{ped} \propto \mu\rho_{tor} s^{\varepsilon}$ and $k_{ped} \approx p / \nabla p$

For ITER Q_{LH} is about 60MW [5].

VIII. Model of the ELMs in TOKES

The Edge Localized Mode model considered here is a cyclic variation of the pedestal parameters, which caused by ballooning instability. The modeling based on a Peeling-Ballooning theory of Type I ELM [34-38]. The ELMs usually appear in H-mode plasma, when due to extensive plasma heating the edge pedestal pressure gradient and, consequently, plasma current grow, approaching some critical unstable values. The instability reveals itself as a repetitive burst of energy and particles at the pedestal area. The numerical modelling of the ELM includes: 1) the ELM triggering conditions, 3) the transport model during and between the ELM burst, 2) mechanism of ELM cycles and typical time scaling, 4) model of energy and particles loss during an ELM. Finally, some numerical results of the ELM simulation, based on simplified model are presented here for the purpose of benchmarking.

VIII. 1. The ELM triggering conditions. When in H-mode of operation power input increases the pedestal pressure gradient raises and can approach the absolute pressure limit (Ballooning limit):

$$\left(\frac{dp}{dx}\right)_c = \frac{B^2 a}{2\mu_0 R}\frac{S(x)}{q(x)^2} f_c \qquad \text{(VIII. 1.1)}$$

where R is the major radius, a is the minor radius, q is the safety factor, B is the magnetic field, and p is the pressure, $S(x)$ is the shear and f_c is some geometrical factor [39]. Once this limit is reached, the transport at the edge turns back to the L-mode (anomalous) value. This can be taken into account by assuming, that the denominator in thermal conductivity coefficient turns to 1.

$$\chi = \frac{\chi_{an}}{1+\mu\theta(Q-Q_{LH})s^2\rho_i/\left(k_{ped}+\Delta_{ped}\right)^2} + \chi_{neo} \le \chi_{an} \qquad \text{(VIII. 1.2)}$$

As a result, the pressure gradient is flattening. At this phase of ELM, energy and particles are expelled to the SOL. These losses occur radially from the stability violation point outwards, assuming quick (with alfven time scale) re-connection of the affected area with the divertor plate. This can be modeled by adding the parallel convective losses of heat and particles in the SOL region: $P_{e,i}^{SOL} + P_{e,i}^{ELM}$, $\Gamma_n^{SOL} + \Gamma_n^{ELM}$

$$P_{e,i}^{ELM} = 2.5 \cdot nT_{e,i}^{ped}/\tau_{//} = 2.5 \cdot nT_{e,i}^{ped} C_S / L_c, \quad \Gamma_n^{ELM} = nC_s / L_c \qquad \text{(VIII. 1.3)}$$

where $L_c \approx \pi qR$ is a connection length and $P_{e,i}$, Γ_n^{ELM} are power and particle sinks due to an ELM, respectively.

The cross-field transport during an ELM burst can be presented as:

$$\chi_{e,i}^{ELM} = \frac{P_{e,i}^{ELM}}{P_{e,i}^{SOL}} \chi_{e,i}^{SOL}, \qquad D_{e,i}^{ELM} = \frac{\Gamma_n^{ELM}}{\Gamma_n^{SOL}} D_{e,i}^{SOL}. \qquad \text{(VIII. 1.4)}$$

This normalization is based on the experimental fact that there is no large difference in the power deposition profile on divertor plates during and between the ELMs. These additional losses and enhanced cross-field transport in the SOL are switching on when at some radial position the stability of ballooning mode is violated and exist until this violation disappears in the whole confinement region.

VIII. 2. Modeling of ELM limit cycle, typical time scales. The described above model gives the following estimate for the ELM affected width of pedestal, δ_{ELM}, the ELM time scale τ_{ELM} and the ELM recovery duration, $1/f_{ELM}$. Where f_{ELM} is the ELM frequency.The fraction of energy stored in the outer part of the pedestal is assumed proportional to Δ_{ped}/a, where Δ_{ped} is the pedestal width and *a* is the plasma minor radius. Only $\delta_{ELM}/\Delta_{ped}$ of this fractional energy would be lost during the ELM event, so that $(\Delta W/W)_0 \approx \delta_{ELM}/a$. For coupled peeling-ballooning modes, the mode width can be expressed as

$$\delta_{ELM} \approx Na/\mathrm{n}qs, \qquad \text{(VIII. 2.1)}$$

where *N* related to the toroidal mode number ~ 2-3, *q* is the safety factor and *s* is the magnetic shear. Finally, the ratio of the energy loss per ELM burst, ΔW, to the energy stored in the pedestal area, W, can be estimated as:

$$(\Delta W/W)_0 \approx N/\mathrm{n}qs \qquad \text{(VIII. 2.2)}$$

For estimation of the ELM burst time two time scales are expected to be relevant. The first is the Alfven time $\tau_A = \pi qR/c_A$, were $c_A = B/\sqrt{\mu_0 n m_i}$ is the Alfven velocity, and the second is the resistive diffusion time across a narrow layer of width, δ_{ELM},

i.e. $\tau_\eta = \mu_0 \delta_{ELM}^2 / \eta$, where η is the plasma resistivity. In principle, τ_{ELM} could involve any combination of these time-scales, and can be written as

$$\tau_{ELM} \approx \tau_A S^p \qquad \text{(VIII. 2.3)}$$

where $S = \tau_\eta / \tau_A$, is the Lundquist number, and *p* is a fractional power (1~1/3). A typical value of the ELM duration τ_{ELM} is usually a few tens/hundreds microseconds.
The ELM duration time is simply inverse proportional to the ELM frequency and for Type I ELM is typically in the range of several tens milliseconds.

Current evolution during the ELM recovery follows the resistive time and described by Ohm law with classical or anomalous resistivity. This time scale must agree with the inverse ELM frequency value. It is reasonable to suggest that the turbulence affects the current evolution, increasing the resistivity at the plasma edge.

The stability diagram for peeling-ballooning mode and an ELM cycle is explained below in Fig.18

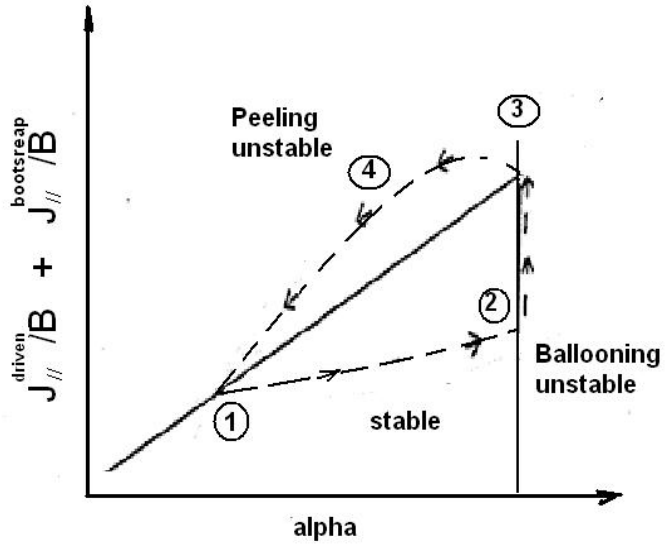

Fig. 18. *Schematics for the peeling-ballooning model and cycling diagram.*

Dimensionless current is plotted against the dimensional pressure. Beyond some alpha value (see vertical line) the ballooning mode is unstable. The inclined line separates the peeling unstable areas.

We begin at the point (1) (see Fig. 18) with low pressure gradient and low current. As we heat the plasma the pressure gradient rises, and we approach the ballooning stability boundary. The current density will also rise, but this will occur on the current diffusion time, which is generally slower than the pressure diffusion time. On reaching the ballooning stability boundary (2), the edge transport would increase effectively tying the pressure gradient to the marginally stable value, but no large scale event is anticipated at this point. Meanwhile, the current will rise on the slower timescale due to the effect of the bootstrap current. Since the peeling mode becomes destabilized, the trajectory will tend to drift up towards the point (3) where the plasma would also become unstable to the peeling mode.

Note, that at this point, the increase in the thermal transport, and subsequent reduction in α, caused by the instability, further destabilizes the mode, leading to a crash event(4). Furthermore, at the point (3) the peeling mode couples to the ballooning mode, so that in this vicinity the mode is rather radially extended (typically ~10% of the minor radius) so that a significant fraction of the pedestal region would be affected by the instability, and as a result a lot of energy would be lost; this can be interpreted as the Type I ELM.

VIII. 3. Transport in the pedestal region during the ELM. On reaching the ballooning boundaries (VIII. 1.1) the edge transport increases, expelling the energy and particles into the SOL region. Pressure gradient at the pedestal position drops back to the marginally stable value. Since the power from the bulk plasma cannot be transferred outwards at that pressure gradient, it starts to increase again up to the critical value α_{cr}, and the process repeats. Two phases must be distinguished: the burst phase of a strong transport increase, reducing eventually the pedestal, and the phase of gradient recovery at the edge. The recovery time scales inverse proportional to the ELM frequency f_{ELM}, $\tau_{ELM} \sim 1/f_{ELM}$, whereas the burst time depends on instability.

VIII. 4. Transport in the scrape-off-layer (SOL) during the ELM. At first phase of ELM, energy and particles are expelled to the SOL. The same happens with the edge current, but in different (resistive) time scale. These losses occur radially from the stability violation point outwards, assuming quick (with alfven time scale) re-connection of the affected area with the divertor plate. This can be modeled by adding the parallel convective losses of heat and particles in the SOL region: $P_{e,i}^{SOL} + P_{e,i}^{ELM}$, $\Gamma_n^{SOL} + \Gamma_n^{ELM}$

$$P_{e,i}^{ELM} = 2.5 \cdot nT_{e,i}^{ped} / \tau_{//} = 2.5 \cdot nT_{e,i}^{ped} C_S / L_c, \quad \Gamma_n^{ELM} = nC_s / L_c \qquad \text{(VIII. 4.1)}$$

where $L_c \approx \pi q R$ is a connection length and $P_{e,i}$, Γ_n^{ELM} are power and particle sinks due to an ELM, respectively. The cross-field transport during an ELM burst can be presented as:

$$\chi_{e,i}^{ELM} = \frac{P_{e,i}^{ELM}}{P_{e,i}^{SOL}} \chi_{e,i}^{SOL}, \qquad D_{e,i}^{ELM} = \frac{\Gamma_n^{ELM}}{\Gamma_n^{SOL}} D_{e,i}^{SOL}. \qquad \text{(VIII. 4.2)}$$

This normalization is based on the experimental fact that there is no large difference in the power deposition profile on divertor plates during and between the ELMs. Between the ELMs the L-mode transport conditions are working. This means, for example, the anomalous transport in the core region with the Bohm type cross-field diffusion and the parallel classical Spitzer-Harm transport in the SOL. These additional losses and enhanced cross-field transport in the SOL are switching on when at some radial position the stability of ballooning mode (VIII. 1.1) is violated and exist until this violation disappears in the whole confinement region.

VIII. 5. Model of energy and particle loss during the ELMs. When an ELM occurs, the pedestal plasma loses energy towards the divertor plate for a time τ_{ELM}. The duration is much shorter than the typical energy equilibration time and, as a consequence, the energy is transported to the divertor mainly at the ion sound speed. The electron flux is impeded by the formation of a strong electric field, which is set up in the plasma over a few ms, when a large population of hot electrons first reaches the target. Consequently, the ELM energy drop is determined by the ratio of the ion parallel energy loss time and the ELM time. Then the fractional energy loss will be, for example, described by:

$$\Delta W / W = (\Delta W / W)_0 \left(1 + \tau_{//} / \tau_{ELM}\right)^{-1} \qquad \text{(VIII. 5.1)}$$

where $\tau_{//}$ is the energy loss time (due to conduction and convection), i.e.:

$$\tau_{//} \approx \pi q R N \left(1 + c_\nu \nu^*\right) / c_s \qquad \text{(VIII. 5.2)}$$

The subscript 0 in (VIII. 5.1) indicates the fractional energy loss, that would occur if the parallel transport timescale were much faster than the ELM timescale. Here ν^* is the electron collisionality, R is the major radius, c_s is the sound speed for the pedestal temperature, and c_ν is the fitting parameter. Due to the magnetic reconnection the connection length is multiplied by some factor N, which further plays a role of the fitting parameter.

Substituting (VIII.5.2, VIII. 2.3) for, $\tau_{//}$, τ_{ELM} into (VIII. 5.1) and using $(\Delta W / W)_0 \approx \delta_{ELM} / a$, one can write down a scaling for the energy loss during an ELM:

$$\Delta W / W = c_w (N / nsq)\left(1 + N(1 + c_\nu \nu^*) / S^p \sqrt{\beta}\right)^{-1} \qquad \text{(VIII. 5.3)}$$

Here $\beta = 8\pi p / B^2$ is the ratio of thermal to magnetic energy in the pedestal, c_w and c_ν are the fitting constants. Fitting parameters $p = 1/3$, $c_\nu = 1$, $c_w = 0.15$, $n = 3$ were obtained by using a least square procedure in comparison with experimental data. Parameter N is taken as 5, to have the best fit.

According to this model, the ELM size and deposition time are dependent on collisionality due to the limitation of the transport time along the open magnetic field lines ("plugging effect") [38,39,40].

VIII. 6. Some numerical results for benchmarking. A simplified stability criterion (VIII. 1.1) for the ballooning mode was adapted in the ASTRA transport code [41]. When total edge current exceeds the peeling limit, then the radial transport coefficient was increased by a large amount within a region of radial width δ_{ELM} at the plasma edge. Fig.19 shows the calculated evolution of plasma temperature and density during and after ELM in JET.

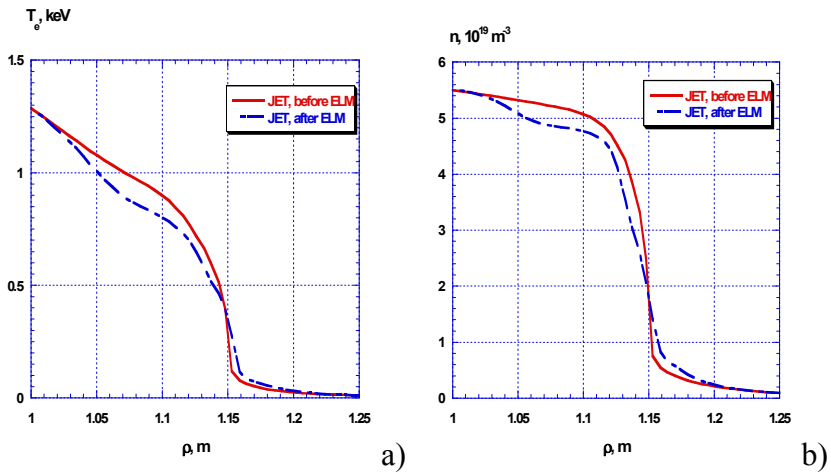

Fig.19. Electron temperature (a) and density (b) profiles before and after ELM (JET case, [45]*).*

Convective losses along the magnetic field lines dominate during the ELM. At $t \geq \tau_{ELM}$ edge current decreases and the plasma becomes stable to both ballooning and peeling modes. The radial transport drops to neoclassical level (see Fig. 19) and convective losses are no longer active.

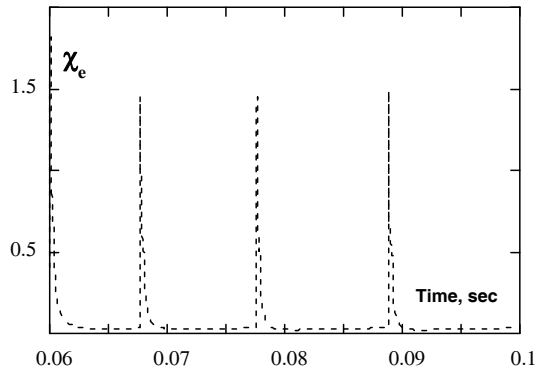

Fig. 20 *Time evolution of the thermal conductivity at the edge during the ELM cycle; m2/sec; min value correspond to* $\chi_{neoclas.}$.

As a result, the pedestal slowly recovers and the plasma again crosses the stability boundary. Clearly in this case a cycle occurs, and we see in Fig. 21-22 the evolution of various equilibrium quantities over a couple of ELM periods.

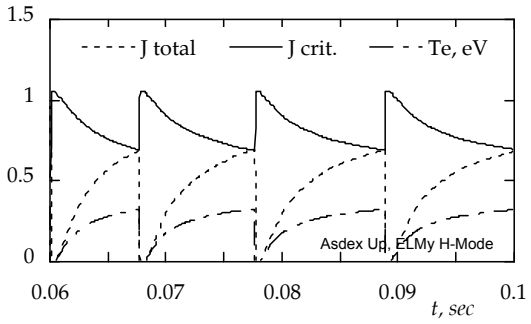

Fig. 21 *Time evolution of the critical (solid) and total currents (short dashed line), MA/m2; pedestal electron temperature Te, keV (long dashed line)*[41,42].

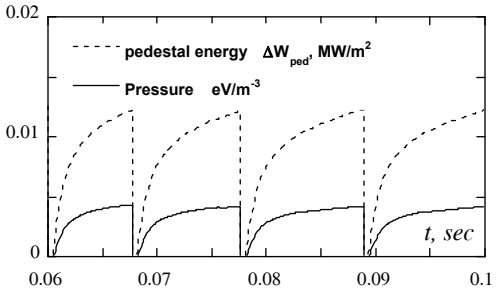

. Fig. 22 *Time evolution of the stored pedestal energy* ΔW_{ped} *(dashed) and total pressure (solid) at the edge* [42,43].

The time scale for ASDEX Up parameters for the ELM is $\tau_{ELM} \approx 400\mu\sec$ and the time between ELMs $\approx 10m\sec$. The energy loss per ELM is estimated as $12 \div 18kJ$, comparable with the experiment data. The transport coefficient $\chi_\perp$ is of the order $1 \div 1.5\ m^2/\sec$. The qualitative agreement with ASTRA data provide confidence in the model. The evolution of the plasma density and the electron and ion temperatures in the case of JET plasma is similar (see Fig.23). The ELM repetition rate in the model is found to be about 15 ms, a factor of 3 smaller than the experimental one (for JET it is about 50 ms). It is seen that during an ELM approximately 1% of the total energy is lost, consistent with the ELM repetition rate, whereas in the experiment the energy loss is about 3%.

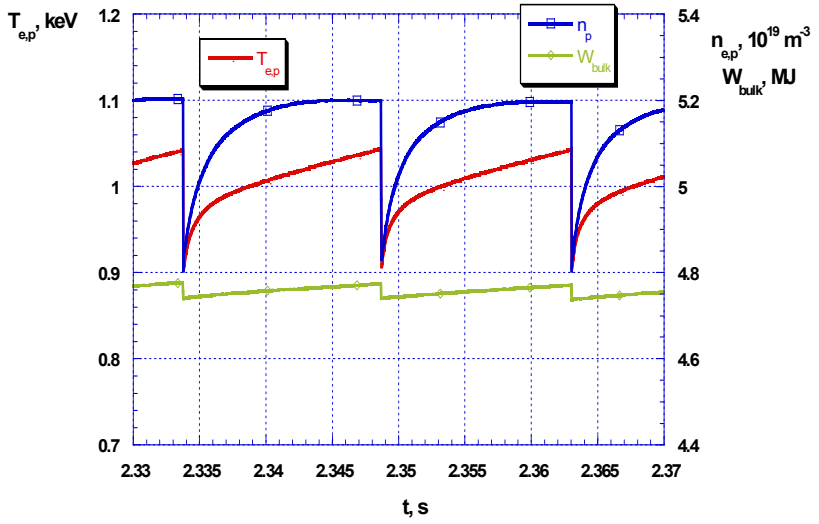

Fig.23. Time dependence of electron temperature and plasma density at the pedestal top and the bulk energy (JET case [45]*). Calculation from* [46]

The results of the computations presented here demonstrate that the model fits the experimental data at least qualitatively. In section VIII the calculation of ELMs in TOKES are presented.

X. Results of calculation in TOKES

X.1 Attached case., plasma parameters in the SOL and divertor

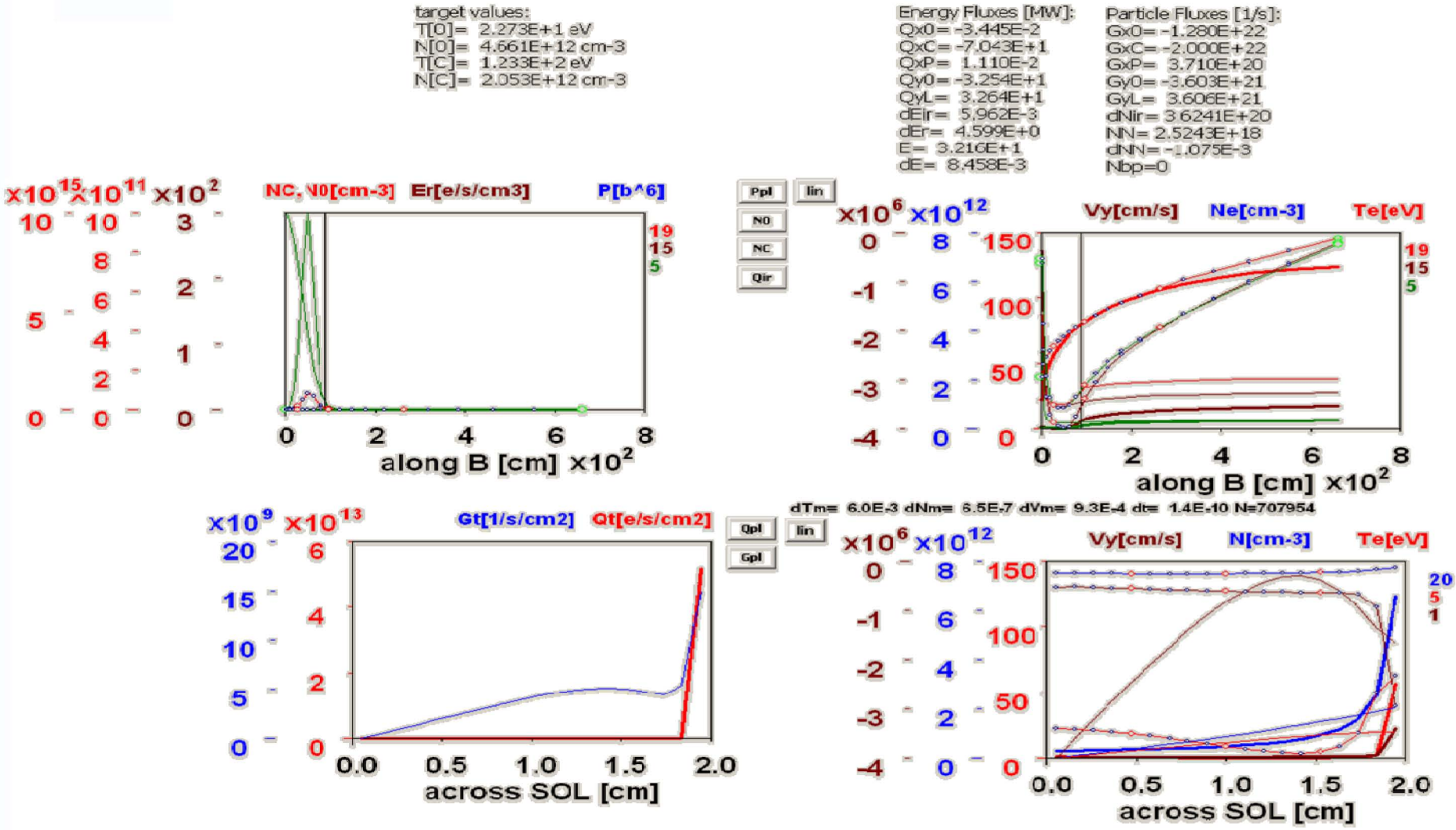

X.2. Partially detached case Plasma parameters in SOL and divertor.

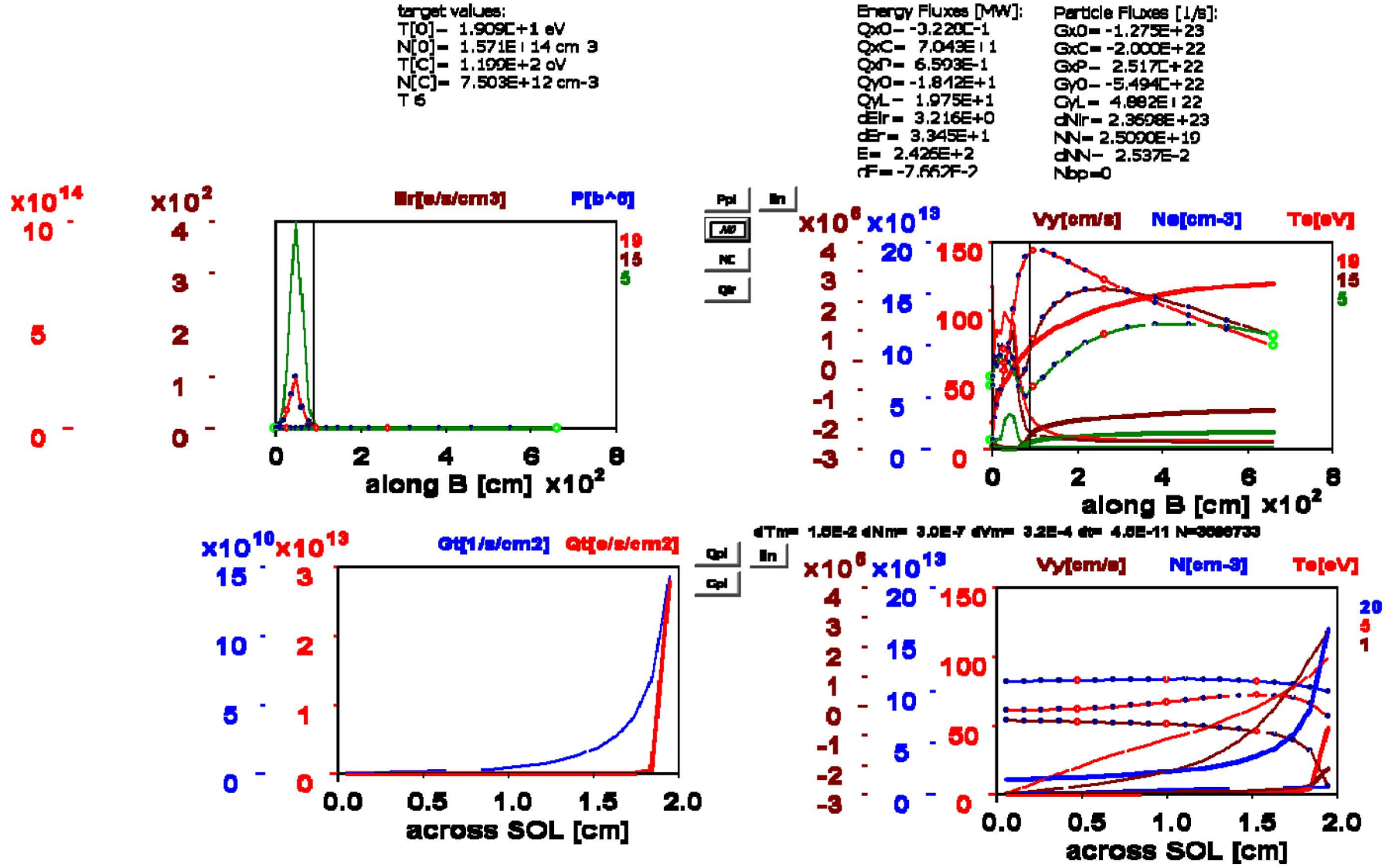

X.3. Fully detached case Plasma parameters in the SOL and divertor.

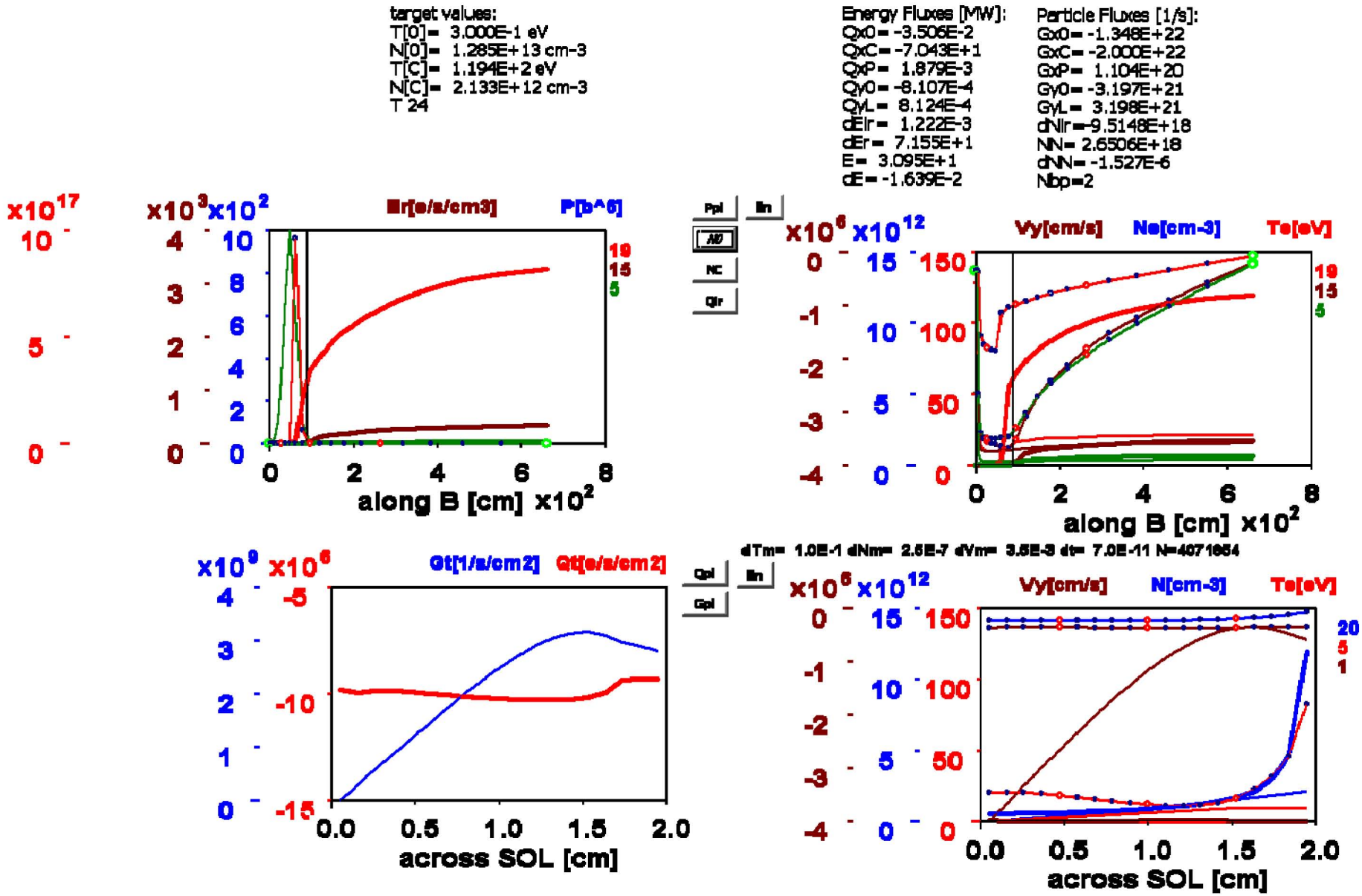

X.4. Core transport and L-H mode transition

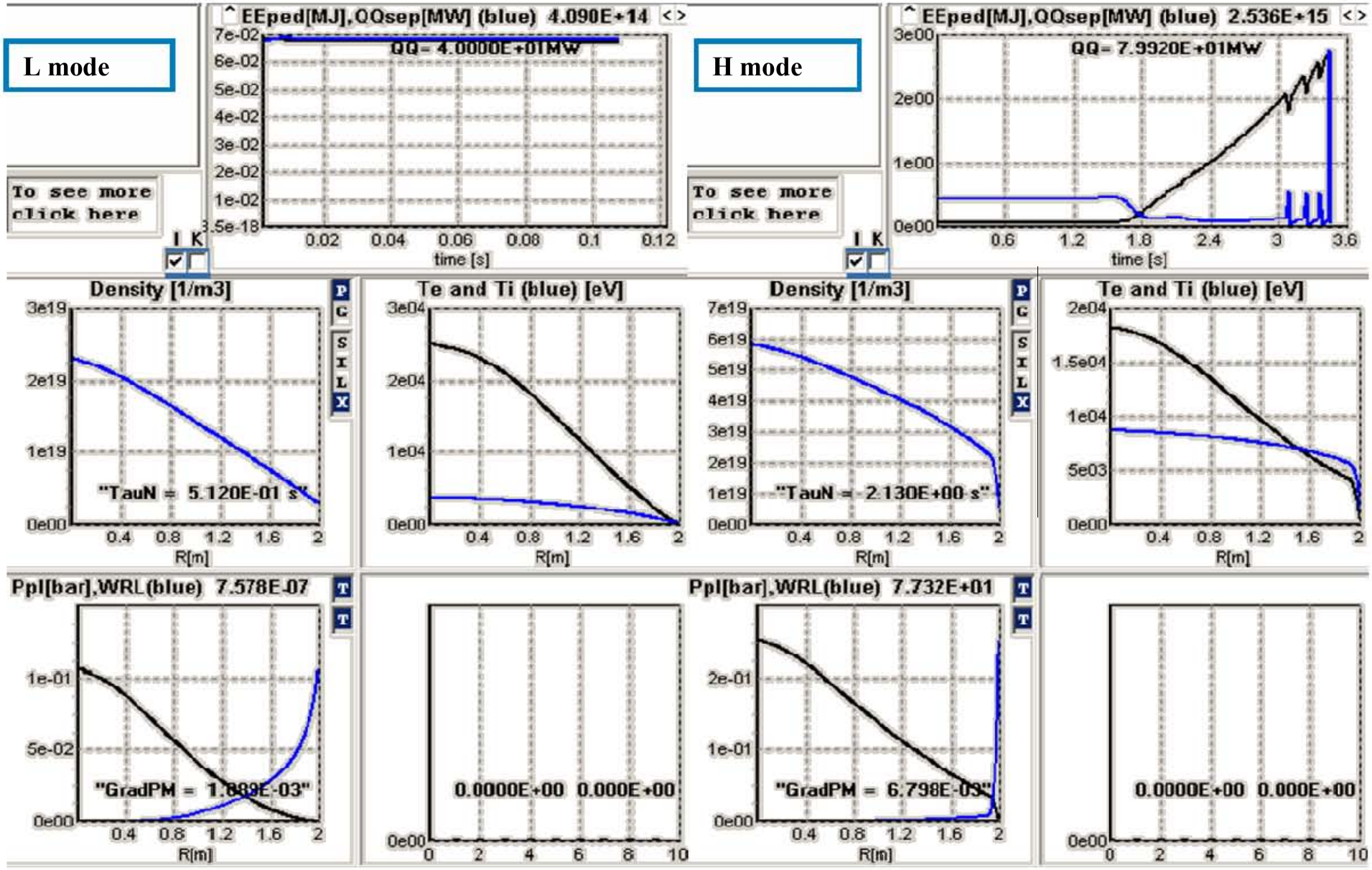

X.5. ELM simulation in TOKES - I

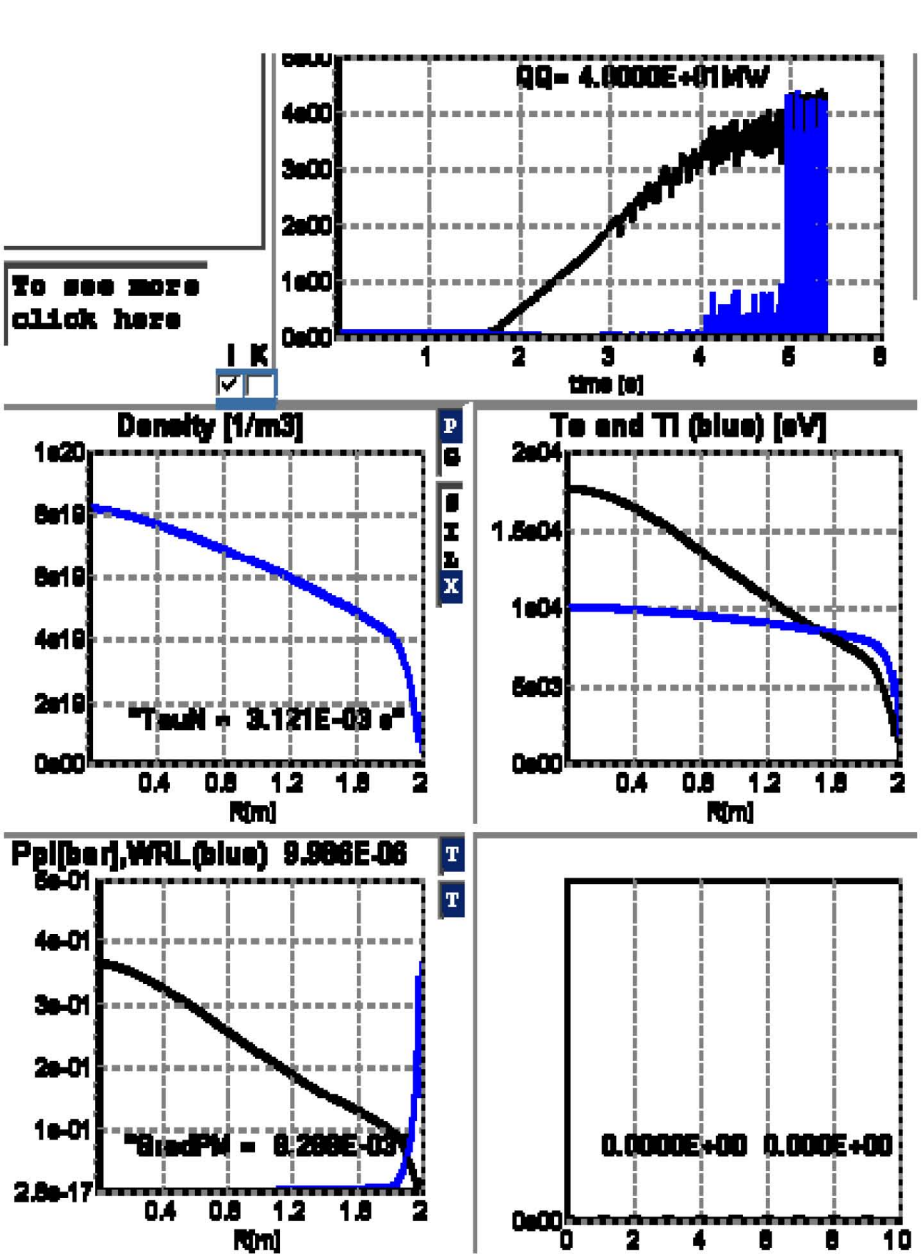

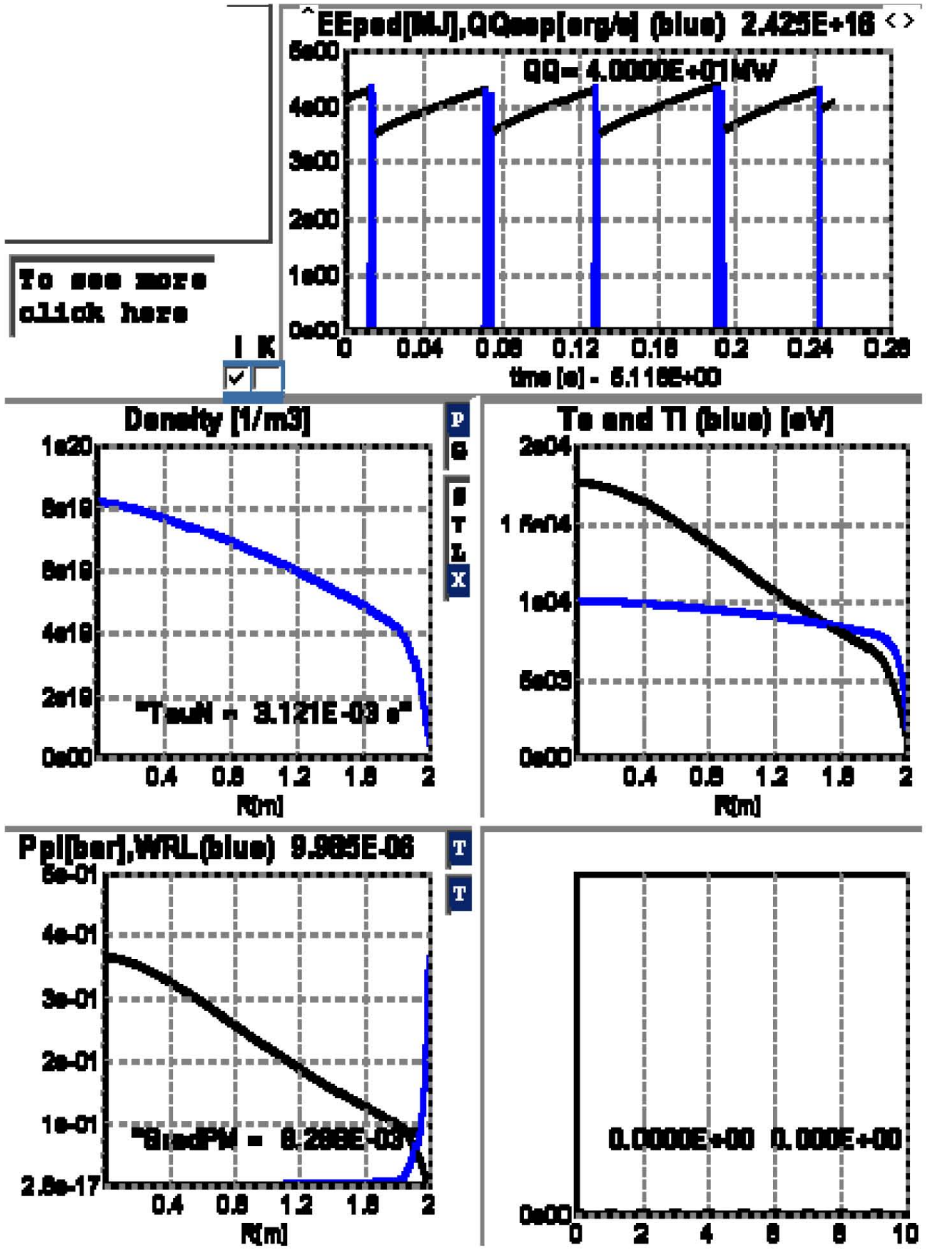

2. ELMs simulation in TOKES -II

profiles comparison:
full core

pedestal
before and after ELM

pedestal
during and after ELM

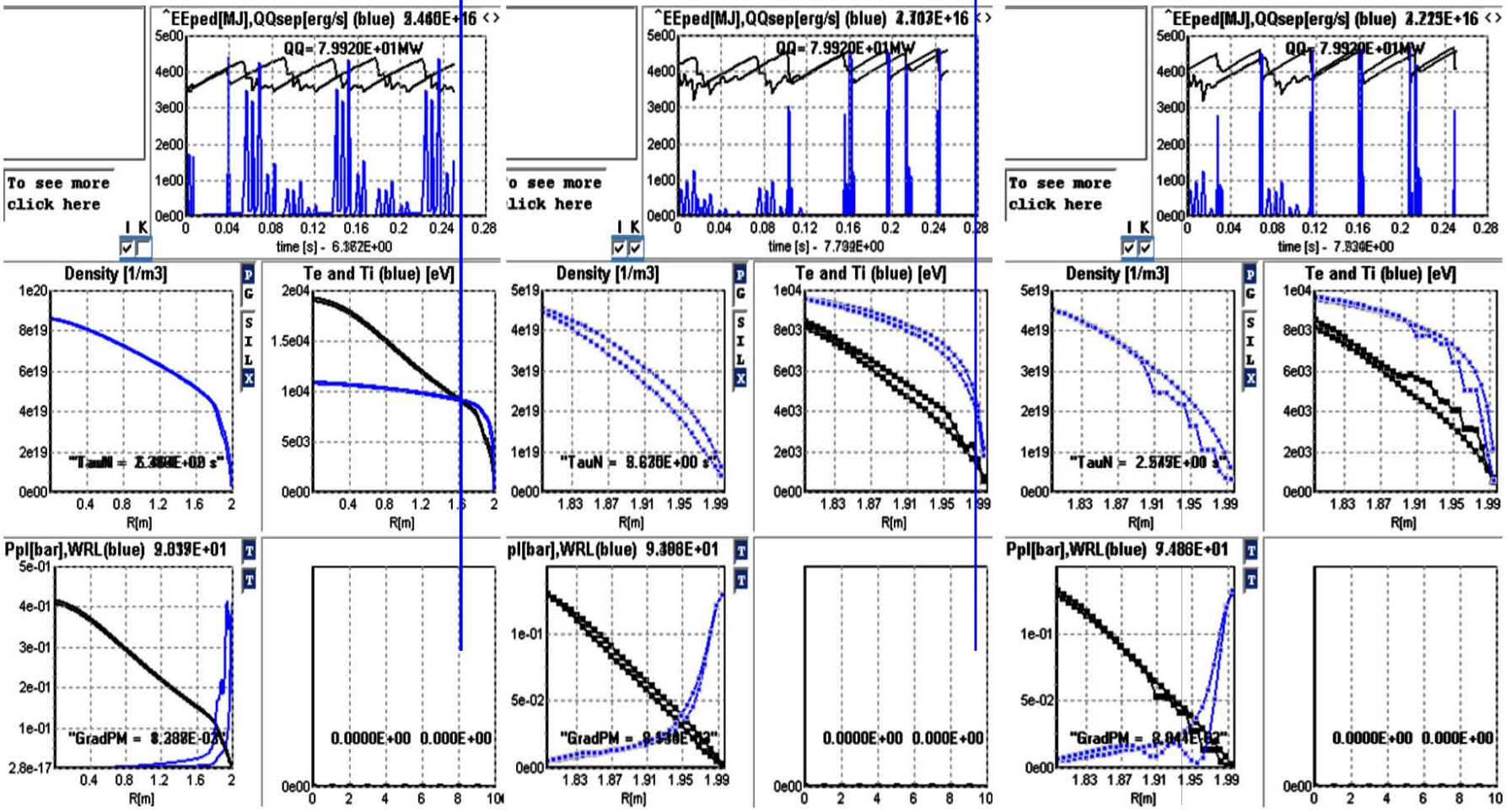

IX. Conclusive remarks and TOKES application for ITER

The main objective of the project was to develop physics-based models of neoclassical and turbulent transport coefficients in the core, pedestal and scrape-off layer/ divertor regions for numerical implementation into TOKES transport code. This ultimate goal has been completed and update TOKES transport code version, suitable for simulation of transient processes (ELMs, Massive Gas Injection etc.) and impurity dynamics in the ITER boundary plasma was prepared. Two physics tasks, related to ITER, are currently under discussion and will be simulated in TOKES.

First task is

a) to evaluate ITER core plasma pollution with tungsten impurities sputtered from the divertor plates by small (mitigated) ELMs during the discharge time. This gives the answer to which extent ELMs have to be suppressed to be tolerable for ITER operation in the sense of PSC life-time and dilution. The model will include a sputtering of divertor plates by incident ELMy hot particles as a source of impurity ions, dynamics of impurity ions in the SOL region and "entraining" effect of ELMs in the pedestal area.

The second task is

b) to simulate the radiation energy distribution on the first wall during TQ and CQ stage in ITER caused by Massive Gas Injection (MGI). Impurities of Ne and Ar will be introduced in H-mode ITER discharge by MGI and their poloidal and radial distribution will be calculated by 2D TOKES Code. Stoping radius and required amount of injected gas will be rescaled for ITER by taking into account results and arguments from JET experiments. Such calculations are 2D and address the poloidal asymmetry in the first instance. TOKES Code will include the 2D impurity transport in the SOL and pedestal region and will account for the opacity effects in realistic (magnetic) geometry.

The following tasks will be implemented in TOKES in near future:

1. plasma current equation
2. current equation for ELM triggering (peeling-ballooning modes interplay)
3. 2D impurity dynamics in the SOL
4. entraining mechanism of impurity screening
5. 2D grid in the pedestal zone
6. diverter plate sputtering by incident ions from the ELM transient loading
7. model for hydrogen dynamics in the boundary plasma; modelling of MGI.
8. poloidal convection, $V_{y,sep}$ and boundary conditions at the separatrix

Acknowledgement

This work, supported by the European Communities under the contract EFDA/05-1305 between EURATOM and Forschungszentrum Karlsruhe, was carried out within the framework of the European Fusion Development Agreement. The views and opinions expressed herein do not necessarily reflect those of the European Commission.

References

[1] Landman,I, Janeschitz,G., Proc. 33rd EPS Conf. on Plasma Physics, Roma, Italy, June 19-23, 2006, ECA Vol. 301, P5.165;

[2] Landman,I, Janeschitz,G, "Numerical simulations of plasma wall interactions for ITER", 17th Intern. Conf. on Plasma Surface Interactions, Hefei Anhui, China, May 22-26, 2006;

[3] Landman,I, Janeschitz,G, J. Nucl. Mater. 363-365, (2007) 1061;

[4] Landman,I, Janeschitz,G " Plasma Convection in ITER Integrated Modelling with the Code TOKES", paper in 34thEPS Conference on Plasma Physics, 2 - 6 July 2007.

[5] ITER Physics Basis, Nucl. Fusion **39** (1999),

[6] Houlberg, W.A., NCLASS from www.pppl.gov/rib/repositories/NTCC

[7] Hinton, F. and R. Haseltine, Rev.Mod.Physics.vol.48.No.2, Part1, 1976

[8] Kotschenreuther, M., Dorland, W. Beer M. et al., Phys. Plasmas **2** (1995) 2381.

[9] Kotschenreuther, M., et al., in Fusion Energy 1996 (Proc. 16th Int. Conf. Montreal, 1996), Vol. 2, IAEA, Vienna (1997) 371.

[10] Helander, P., Fülöp, T. (1999). Nonlinear neoclassical transport in a toroidal plasma with large gradients. *26th EPS , Maastricht*. 23J s. 25

[11] Rebut, P., Lallia, P., Watkins, M., IAEA, Proc. 12th Intern. Conf., Nice, 1988, p.191.

[12] Ottaviani, M., Horton, W., Erba, M., Plasma Phys. Control. Fusion **39** (1997) 1461.

[13] Biglari H, Diamond P H, Terry P, Phys. Fluids-B 1990 *2* 1-4**.**

[14] Pogutse O., Igitkhanov Yu. *et al.*: *Proc. 24th EPS*, Berchtesgaden, 1997, III, p. 1041

[15] Braginski S.I., Reviews of plasma physics (ed. Leontovich, M.A.),Vol. 1, Consaltants Bureau, New York (1965).

[16] Boley C., Gelbard E., and HirshmanS., Phys Fluids 22(7), July 1977

[17] Bergmann A., Igitkhanov Yu., Braams B., Coster D., Schneider R. Contributions to Plasma Physics, vol. 36, issue 2-3, pp. 192-196

[18] Sagdeev R.and Galeev A.,1970, Sov. Phys.-Docl.14, 1198

[19] Igitkhanov yu., Kukushkin A., Pigarov Yu., Pistunovich V., Sov. J. Plasma Physics12(1) January 1986

[20] Igitkhanov Yu. and Yushmanov P., Contr. Plasma Phys.30 (1988) 341.

[21] Игитханов Ю. Л., Крашенинников С. И., Кукушкин А. С., Юшманов П. Н.. Особенности процессов переноса в пристеночной плазме токамака // Итоги науки и техники. Сер. Физика плазмы. Т. П. М.: ВИНИТИ, 1989. С. 6-149]

[22] Kukushkin A., Runov A., Contr. Plasma Phys., 34 (1994) 204

[23] Loarte A. et al,. Physica Scripta T128 (2007) 222-228.

[24] Bazylev et al, B.Physica Scripta. T128, 229 (2007).

[25] Zhitlukhin] A. et al, J. Nucl. Mat. 363-365, 301 (2007).

[26] Bazylev B.et al, J. Nucl. Mater. 337-339 (2005) 766-770.

[27] Olson, Lorraine G., et al., Journal of Computational Physics 96 (2): 391-410.

[28] Bazylev B., Igitkhanov Yu, Janeschitz G., I. Landman, Simulation of hot-spot formation at ITER vessel surface during multiple transient events**,** 35th EPS Conference**,** Hersonissos, Crete, June 9 - 13, 2008

[29] Marchetti S. et.al., IEEE Transactions on Antennas and Propagation, vol.38, 9,1990 Antennas and Propagation, vol.38, 9,1990

[30] Самарский А.А. Теория разностных схем. - М.: Наука, 1979, с.656

[31] Samarskii, A.A., Nikolajev E.S., Methods for Solving Difference Equations, Nauka, Moscow, 1978

[32] Belotserkovski O., Davidov Yu., Large Particle Method in Gas Dynamics, Nauka, Moscow (1982), (in Russian)

[33] Sugihara M., Igitkhanov Yu., Janeschitz G., et al., "Studies on the Scaling of H-mode Pedestal Width in the ITER Multi-machine Pedestal Database", Proc. of 26th EPS Conf. on Cont. Fusion and Plasma Physics **(**Maastricht), **23J** 1449 (1999).

[34] Connor, J.W., et al., in Fusion Energy 1996 (Proc. 16th Int. Conf. Montreal, 1996), Vol. 2, IAEA, Vienna (1997) 935. 506 Nuclear Fusion

[35] Connor J.V., Hastie R.J., Wilson H.,R., Physics of Plasmas, 5 (1998) 2687

[36] Connor et.al., Phys Rev Lett 40 (1978) 396

[37] Manickam, J., Phys. Fluids B 4 (7), July 1992 , p. 1901

[38] Wilson, H.R., Connor, J.W., et al., 17th IAEA Fusion Energy Conference, IAEA-F1-CN-69/TH3/2, Yokohama (1998).

[39] Janeschitz G., et al., paper on 14th PSI, J. Nucl. Mat., Rosenheim, Germany, 2000

[40] Janeschitz, G., Igitkhanov, Yu., Sugihara, M., et al., 26 the EPS, Maastricht, 1999.

[41] Pereverzev, G.V., et al., ASTRA: Rep. IPP 5/42, Max-Planck-Institut fuer Plasmaphysik, Garching (1991).

[42] Igitkhanov Yu.et al., 28th EPS. No P4.101,2001

[43] Sugihara, M., Igitkhanov, Yu., Janeschitz, G., et al., 26th EPS, Maastrich, 1999.

[45] Loarte A., et al., 18th IAEA 2001.

[46] Zolotukhin O. et al., 28th EPS, Cont.No.P2.051,2001